Initialization and Validation of a Simulation of Cirrus Using FIRE-II Data

D. L. WESTPHAL,* S. KINNE,+ P. PILEWSKIE,+ J. M. ALVAREZ,# P. MINNIS,# D. F. YOUNG,# S. G. BENJAMIN,@ W. L. EBERHARD,& R. A. KROPFLI,& S. Y. MATROSOV,& J. B. SNIDER,& T. A. UTTAL,& A. J. HEYMSFIELD,** G. G. MACE,++ S. H. MELFI,## D. O'C. STARR,## AND J. J. SODEN@@

*Naval Research Laboratory, Monterey, California
+NASA/Ames Research Center, Moffet Field, California
#NASA/Langley Research Center, Hampton, Virginia
@NOAA/FSL, Boulder, Colorado
&NOAA/ETL, Boulder, Colorado
**NCAR, Boulder, Colorado
++Pennsylvania State University, University Park, Pennsylvania
##NASA/Goddard Space Flight Center, Greenbelt, Maryland
@@NOAA/GFDL, Princeton, New Jersey

(Manuscript received 4 January 1996, in final form 10 June 1996)

ABSTRACT

Observations from a wide variety of instruments and platforms are used to validate many different aspects of a three-dimensional mesoscale simulation of the dynamics, cloud microphysics, and radiative transfer of a cirrus cloud system observed on 26 November 1991 during the second cirrus field program of the First International Satellite Cloud Climatology Program (ISCCP) Regional Experiment (FIRE-II) located in southeastern Kansas. The simulation was made with a mesoscale dynamical model utilizing a simplified bulk water cloud scheme and a spectral model of radiative transfer. Expressions for cirrus optical properties for solar and infrared wavelength intervals as functions of ice water content and effective particle radius are modified for the midlatitude cirrus observed during FIRE-II and are shown to compare favorably with explicit size-resolving calculations of the optical properties. Rawinsonde, Raman lidar, and satellite data are evaluated and combined to produce a time–height cross section of humidity at the central FIRE-II site for model verification. Due to the wide spacing of rawinsondes and their infrequent release, important moisture features go undetected and are absent in the conventional analyses. The upper-tropospheric humidities used for the initial conditions were generally less than 50% of those inferred from satellite data, yet over the course of a 24-h simulation the model produced a distribution that closely resembles the large-scale features of the satellite analysis. The simulated distribution and concentration of ice compares favorably with data from radar, lidar, satellite, and aircraft. Direct comparison is made between the radiative transfer simulation and data from broadband and spectral sensors and inferred quantities such as cloud albedo, optical depth, and top-of-the-atmosphere 11-μm brightness temperature, and the 6.7-μm brightness temperature. Comparison is also made with theoretical heating rates calculated using the rawinsonde data and measured ice water size distributions near the central site. For this case study, and perhaps for most other mesoscale applications, the differences between the observed and simulated radiative quantities are due more to errors in the prediction of ice water content, than to errors in the optical properties or the radiative transfer solution technique.

1. Introduction

Much of the uncertainty in global climate prediction is due to the use of inaccurate parameterizations of clouds. To improve these models, the current research trend is toward the use of explicit cloud parameterizations instead of diagnostic schemes (Fowler and Randall 1994). Three approaches can be taken in the validation of these new and improved parameterizations. In the first, model diagnostics such as low cloud amount or outgoing longwave radiation (e.g., Slingo et al. 1989) are compared with observations. However, an inaccurate model process is difficult to identify since these second-order parameters depend on many processes in the climate model. The validation is further obscured when the parameter is longitudinally or seasonally averaged. As models and observation techniques become more sophisticated, it is necessary to validate them using quantities that are more fundamental and are averaged over smaller spatial and time scales.

Recently, a second approach, called Single Column Modeling, has been invoked wherein the cloud and radiation parameterizations of a general circulation

Corresponding author address: Dr. Douglas L. Westphal, Naval Research Laboratory, 7 Grace Hopper St., Stop 2, Monterey, CA 94943.
E-mail: westphal@nrlmry.navy.mil

model (GCM) are extracted and, in the vertical dimension, driven by specified large-scale forcing and boundary conditions for hours or days at a time. The resulting predictions are then compared with cloud and radiation observations averaged over a GCM grid cell (~200 km) several times a day (e.g., Iacobellis and Somerville 1991; Randall et al. 1996). This method allows an isolated evaluation of the characteristics of current GCM model physics and may eventually yield improvements to the GCM. It also eliminates the need for initialization over synoptic scales. The major difficulty lies in accurately determining the synoptic forcing (e.g., divergence and the resulting vertical velocities) that contains only those scales of motion that are resolved by the parent GCM. The required observations may be available during special observing periods such as those at the Atmospheric Radiation Measurements (ARM) Cloud and Radiation Testbed (CART) site in Oklahoma (Stokes and Schwartz 1994).

A third approach utilizes synoptic or mesoscale simulations of observed cloud systems using models that have the resolution that GCMs are anticipated to have in the near future; that is, grids that are tens of kilometers on a side and a fraction of a kilometer deep. This approach provides an economical test bed for new and improved parameterizations.

Previous three-dimensional mesoscale studies of ice microphysics include those by Zhang (1989), Levkov et al. (1992), and Heckman and Cotton (1993). Each of these has different goals and uses different models. Zhang used a simplified bulk water model in a nested mesoscale model for a sensitivity study of the influence of ice microphysics in the development of a mesoscale convective system. Radiative transfer was not the focus of this study and a simple radiation parameterization was used. In another sensitivity study, Levkov et al. applied a cloud model of cirrus and stratus and radiation to an idealized case study from the International Cloud Experiment 1989. They investigated the response of the developing clouds to different external perturbations. Heckman and Cotton used a bulk water model in a nested mesoscale model to study the sensitivity of a midlatitude cloud system to radiative and condensational heating.

This paper also uses the mesoscale case study approach for an investigation of a cloud system observed during FIRE-II, the second cirrus field program of the First International Satellite Cloud Climatology Program (ISCCP) Regional Experiment centered over Coffeyville (COF) in southeast Kansas from 13 November to 6 December 1991. The objectives of FIRE-II were to expand our understanding of cloud processes, improve the capabilities of models to simulate clouds, and improve cloud retrievals from remotely sensed data.

The mesoscale case study approach faces difficulties since accurate initial conditions over regional or synoptic scales are required. For the cirrus case study described in this paper, the initialization problem is particularly difficult since upper-tropospheric observations and analyses of water vapor are poor. The validation step for mesoscale case studies also requires cloud and radiation observations over regional or synoptic scales.

These initialization and validation data are available for FIRE-II. It was found in FIRE-I that the mesoscale structure of cirrus cloud fields could not be explained by conventional diagnostic analyses (Starr and Wylie 1990). Also, a regional view was found to be necessary for understanding the surface, aircraft, and satellite cloud observations made during the wide variety of synoptic patterns in which cirrus are found, including dissipating cirrus in northwesterly flow downstream of a ridge, cirrus forced by traveling disturbances, and subtropical cirrus (note the variety of cirrus patterns in Fig. 1). Accordingly, the FIRE-II science plan included mesoscale modeling as a means to understand and quantify the mesoscale forcing and the history of air volumes sampled at COF, along flight tracks, and in regions covered by satellite sensors. In large part, the FIRE-II location was chosen because of its proximity to the center of the National Oceanic and Atmospheric Administration (NOAA) Wind Profiler Demonstration Network (WPDN) with the expectation that accurate hourly records of vertical velocities could be derived from the wind profiler data (e.g., Mace et al. 1995). During episodes of special interest, called Intensive Observing Periods, or IOPs, rawinsondes were released at National Weather Service (NWS) sites and four additional sites at 6-h and 3-h intervals to better resolve the atmosphere, particularly the moisture field. For large-scale analyses, FIRE-II relied on NOAA's Mesoscale Analysis and Prediction System (MAPS; Benjamin et al. 1991) for four-dimensional data assimilation (FDDA) of aircraft, surface, wind profiler, and asynoptic NWS rawinsonde releases during the field program. Since 1991, MAPS has undergone a large number of changes. A much improved 60-km 25-level version was implemented in September 1994 as an operational model (the rapid update cycle) at the National Centers for Environmental Prediction (NCEP; Benjamin et al. 1994, 1995). The version used at the time of the FIRE experiment is described in Benjamin et al. (1993). These data are suitable for initialization of mesoscale models and are also used for validation, as are the unassimilated data from numerous surface-based, airborne, and satellite instruments.

This work is different from previous mesoscale efforts in that the details of the initial conditions, particularly those of the moisture field, are evaluated and a greater emphasis is put on quantitative verification of the cloud and radiation aspects of the simulation. The suite of models employed here allows comparison with a large number of observed and inferred cloud and radiation fields, for example, precipitable water, ice water content, effective particle radius, and 11-μm brightness temperatures at the surface and at the top of the at-

mosphere, in addition to the usual dynamical variables. Rather than comparing to "typical" values observed over the course of the experiment, quantitative comparison with two-dimensional analyses are used, for example, cross sections, time sections, and horizontal views, whenever possible. While a sensitivity study of the large number of free or user-specified parameters involved in the components of the modeling system will be valuable, this task is not carried out in this paper. Instead, the standard assumptions are explained and applied and the resulting simulation is presented. This groundwork must be completed for this case study before the other mesoscale modeling goals of FIRE-II (development of improved microphysical and radiative transfer parameterizations) can be achieved. Sensitivity studies and refinement of the models will be done in a subsequent paper.

In the next section, the modeling system is discussed with an emphasis on the optical properties used in the radiative transfer code. The synoptic setting of the study period is described in section 3. Section 4 contains an evaluation of the initial dynamical conditions and the 24-h dynamical simulation. The observed water vapor distribution is presented and compared with the simulated fields in section 5. The observations and simulations of clouds are compared in section 6. The radiative properties of the observed and simulated clouds are presented and compared in section 7. The conclusions are presented in section 8.

2. Description of the model

The numerical model used in the simulations consists of dynamical, cloud, and radiative components. These have been documented extensively in the literature and only a brief description of each component is given here.

a. Dynamical model

The Pennsylvania State University/National Center for Atmospheric Research (PSU/NCAR) hydrostatic mesoscale model (MM4; Anthes et al. 1987) is used as the dynamical component of the combined model. The horizontal grid length is 60 km, and the vertical grid length varies from roughly 0.5 km near the surface to 1.5 km near the tropopause. The model domain is shown in Fig. 2 and corresponds to the original MAPS domain less two rows of grid points along the four boundaries. Domain nesting was not employed in this study, though some of the figures will show only a subset of the domain and should not be confused with nested domains.

b. Water vapor initialization

Though water vapor is the third most common atmospheric constituent, it is difficult to measure accurately on an operational basis over large areas. Accurate regional or synoptic analyses are difficult to obtain. The quality is particularly bad for initialization of midlatitude winter simulations since the rawinsonde humidity sensors have the greatest difficulty at cold temperatures. At the temperatures and pressures typical of cirrus, an error of 50% in relative humidity with respect to ice RH_i represents an error of approximately 0.75 km in the lifting condensation level. Errors of this size are common for this case study and, coupled with the weak large-scale vertical velocities, of order 5 cm s^{-1}, typical of the cirrus systems studied in FIRE-I and FIRE-II, could lead to errors of over four hours in the simulated time of cloud formation.

In addition to direct effects on clouds, errors in the water vapor amounts cause significant errors in calculations of radiative transfer. Under the clear, cold midlatitude conditions of FIRE-II, a 50% error in the precipitable water (the vertical integral of the mixing ratio over the depth of the atmosphere) causes a modest 5% change in the broadband fluxes at the surface and top of the atmosphere. However, the same 50% error in precipitable water can cause a 50% change in the downwelling flux at the surface in the window region of the spectrum. Obtaining accurate simulations of the spectral observations is difficult under these conditions.

Thus, one of the goals of FIRE-II was to determine the three-dimensional distribution of water vapor and clouds for use in one-dimensional radiative calculations and in initializing and validating numerical models. However, no single special observation technique that was utilized in FIRE-II provides the accurate, regional distributions of water vapor required for this modeling work. The aircraft provide in situ measurements of water vapor, cloud, and ice for hours at a time but only along the flight path. The Raman lidar provides accurate measurements, but only at COF (Fig. 2), for levels up to 10.3 km above sea level (ASL), and during nighttime hours. Inspection of Cross-Chain Loran Atmospheric Sounding System (CLASS) rawinsonde data reveals more sensitivity at cold temperatures than the NWS rawinsondes, but the cold-temperature accuracy is disputed and the four CLASS stations staffed during FIRE-II cover an area that is only 200 km on a side. Supplemental rawinsonde releases were made at most NWS stations, but these are widely spaced and suffer from the problems described in Wade (1991) and D. Westphal (1996, manuscript submitted to *J. Atmos. Oceanic Technol.*). Satellite sensors offer a hope of higher horizontal and temporal resolution but lack the vertical resolution sufficient for model initialization (e.g., Soden and Bretherton 1993).

FIRE-II anticipated the need for data assimilation of the different moisture measurements in order to alleviate the lack of a comprehensive water vapor capability and chose to rely on the Mesoscale Analysis and Prediction System (MAPS) analyses, a 3-h intermittent data assimilation and forecast system. MAPS combines its previous 3-h forecast with the available synoptic and

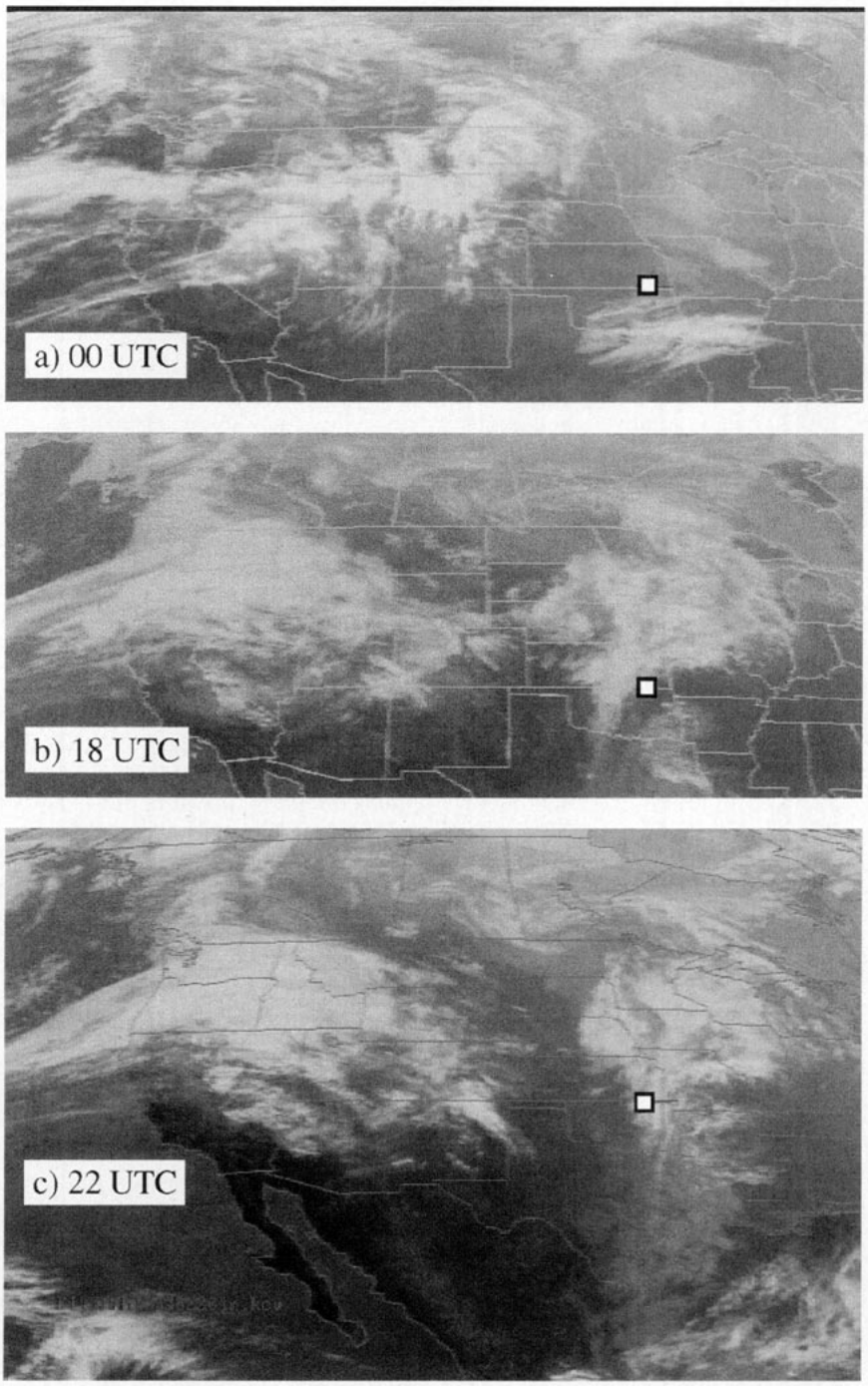

FIG. 1. GOES infrared imagery for 26 November 1991 at (a) 0000 UTC, (b) 1800 UTC, and (c) 2200 UTC.

asynoptic observations such as wind profiler data and automated aircraft reports to produce an updated analysis (Benjamin et al. 1991). During FIRE-II, selected NWS stations made supplemental 3-h and 6-h rawinsonde releases. These data were included in the MAPS assimilation cycle. Data collected at special NCAR CLASS rawinsonde sites were not assimilated by MAPS and represent an independent dataset that can be used to verify MAPS. If measured in terms of rms height errors (and other metrics), the MAPS analyses generally fit the observations more closely than the nested grid model (NGM) analyses available at that

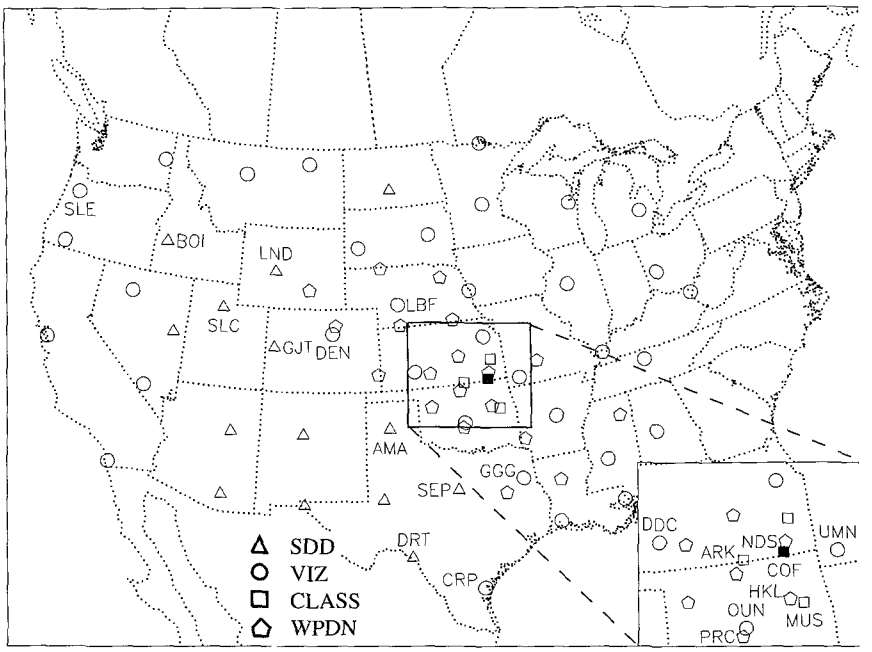

FIG. 2. Extent of model domain used in the simulations described in this paper and locator map for NWS stations that made special releases during FIRE-II (SDD sondes: triangles, and VIZ sondes: circles), NCAR CLASS rawinsonde sites (squares), and NOAA WPDN wind profilers that operated during FIRE-II (pentagons). Coffeyville, Kansas (COF), is represented by the filled square near the center of the domain. The three-letter station indentifiers are given for stations referenced in the text.

time. Unfortunately, the MAPS analyses in the upper troposphere had a dry bias at this time, primarily a result of setting the rawinsonde relative humidity to 5% when the actual rawinsonde moisture observation was missing (generally at levels above 400 hPa). For this reason, MAPS relative humidity *forecasts* from the 1991 version often showed more reasonable upper-level moisture fields than did the *analyses*. This dry bias is illustrated later in this paper and was statistically evaluated by Cairns et al. (1993) for April 1991. However, they also found dry and moist biases of similar magnitudes in the National Meteorological Center's (NMC) eta model, which used the NGM for initialization.

The model is initialized with the MAPS analyses for 0000 UTC 26 November and continues until 0000 UTC 27 November 1991. (Except when noted, all UTC times in this paper will refer to 26 November 1991.) The intermediate 3-h MAPS analyses are used to determine boundary conditions. Several reasons precluded the more economical approach of beginning the simulation nearer to 1800 UTC when the intensive observations began. Although the 1991 version of MAPS did utilize a partial geostrophic constraint in the objective analysis, there was still significant imbalance between mass and wind fields. For example, the 0000 UTC MAPS analyses of 300-hpa geopotential heights and winds are shown in Fig. 3a. While the analyzed winds compare favorably with the available rawinsonde and wind profiler data, the height field exhibits noise particularly over the central Rocky Mountains. The model was not initialized at 0600, 0900, or 1200 UTC since the MAPS analyses for these times contained spurious northerly and northeasterly winds along the Nebraska–Kansas border that contradict the rawinsonde and wind profiler observations (not shown). Thus, beginning the simulation at 0000 UTC allows the mass and momentum fields to adjust, avoids the 0600–1200 UTC analyses, and has the beneficial effect of allowing the model to spin up a reasonable moisture field.

c. *Cloud model*

A bulk water (BW) scheme is used to predict mass concentrations of cloud, ice, rain, snow, and vapor. It eliminates the explicit treatment of the size distribution of ice, droplet, and condensation nuclei by specifying the size distribution and then analytically calculating the bulk conversion rates and fall velocities for the entire population of hydrometeors. In the implementation used here (Zhang 1989), only two classes of hydrometeors are considered: cloud/ice and rain/snow. Temperature is used to distinguish cloud from ice and rain from snow. Although mixed-phase clouds were observed at other times during FIRE-II, the microwave

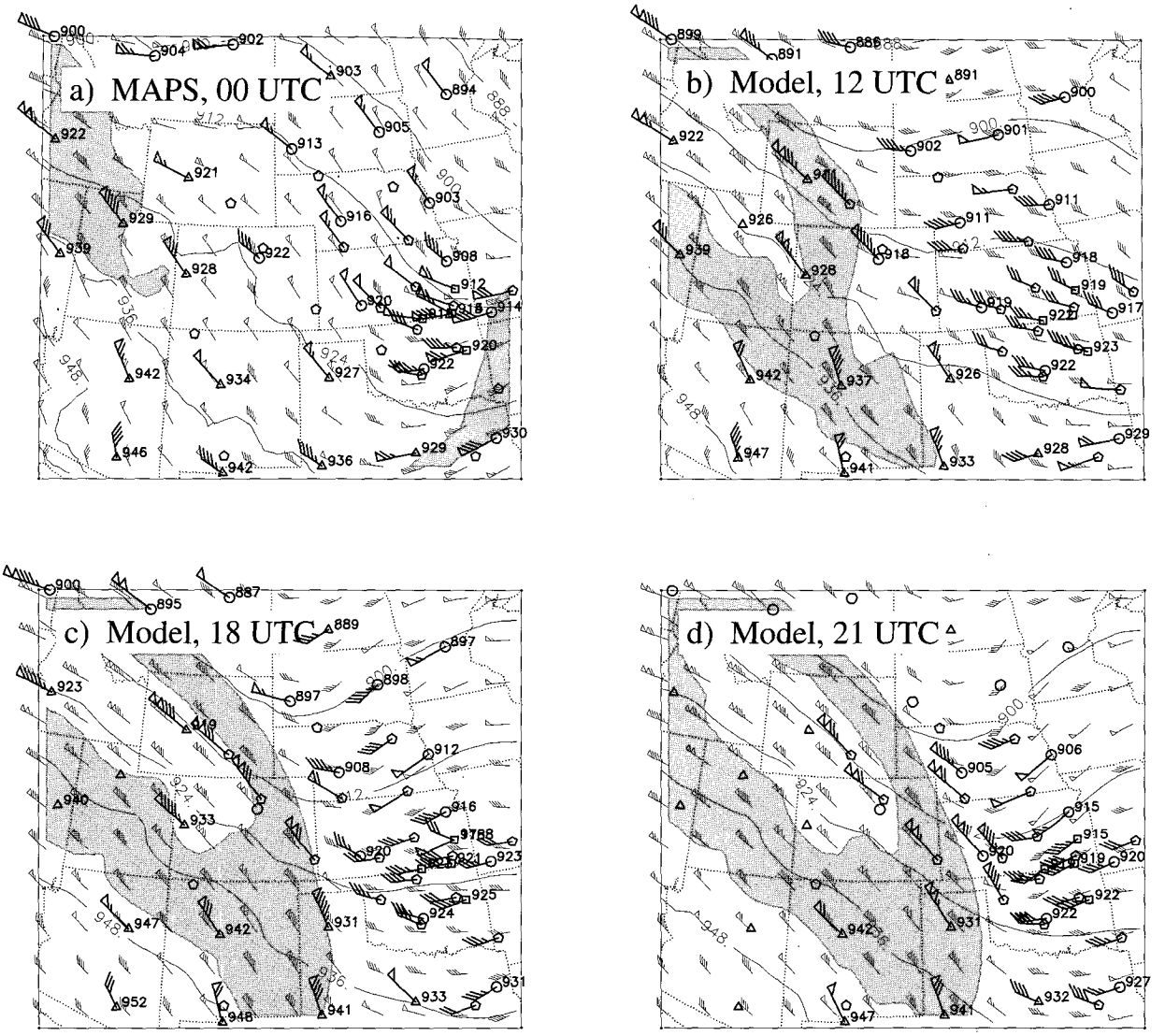

FIG. 3. The 300-hPa geopotential height (solid lines, contour interval of 12 dm) and wind speed for (a) MAPS analysis at 0000 UTC, used as the model initial condition; (b) simulation at 1200 UTC; (c) simulation at 1800 UTC; and (d) simulation at 2100 UTC. Wind barbs are plotted at every third model grid point. One flag equals 25 m s^{-1} and one full barb equals 5 m s^{-1}, so that the representation of wind is nearly identical to that of the knot barbs in the NMC analyses shown in Fig. 6. The region with wind speeds between 36 and 56 m s^{-1} (70 and 110 knots) has been shaded for easy comparison with the shaded region in the NMC analyses. Winds and heights for NWS rawinsondes (triangles and circles), NCAR CLASS rawinsondes (squares), and NOAA WPDN wind profilers (pentagons) are shown in boldface. Data from Purcell, Oklahoma (PRC); Haskell, Oklahoma (HKL); and COF have been purposely deleted to reduce clutter when nearly identical to the data at nearby stations, namely Norman, Oklahoma (OUN); Muskogee, Oklahoma (MUS); and NDS, respectively.

radiometer at COF showed only small amounts of liquid water on 26 November suggesting that mixed-phase microphysics may have been unimportant at COF on this day.

d. Radiative transfer model

The Ames Research Center's (ARC) two-stream radiative transfer code (Toon et al. 1989) is used to calculate radiative fluxes and heating rates. To account for the spectral dependency of clouds and gas radiative properties, the solar and infrared spectral regions are divided into 26 and 18 spectral intervals, respectively. This allows accurate representation of the wavelength dependence of the optical properties of gases and hydrometeors and allows direct comparison of the simulated fluxes and intensities with spectral measurements. Absorption by atmospheric gases for each interval is treated with exponential sum fitting. Molecular absorption is based on Rothman et al. (1983) and the infrared continuum absorption by water vapor is based on Roberts et al.

(1976). Radiative effects of volcanic or other aerosols are not considered since significant amounts were not present on 26 November.

Absorption and scattering by liquid water or ice cloud particles are prescribed for each spectral interval by the three single-scattering properties: the volume extinction coefficient β_e, the single-scattering albedo ω_0, and the asymmetry parameter g. In addition to the spectral dependency, these three properties also depend on particle shape and size. An approach that is practical for use in dynamical models is to represent these three optical properties with constants or expressions that depend on either water content alone or on water content and an effective particle radius r_e (e.g., Rockel et al. 1991; Ebert and Curry 1992; Sun and Shine 1994). The effective particle radius defines a characteristic size of a particle distribution as the ratio of the total volume of a size distribution to its total surface area. The approximations are derived by fitting curves to results from explicit analytical calculations for idealized and observed size distributions. This approach eliminates the need for explicit integrations over particle size during a simulation. However, the assumed size distributions used in the calculation of the optical properties are different from those used in the calculation of the bulk microphysical processes. Thus, the radiative effects and cloud microphysics are decoupled: modifications in the assumed size distribution of one does not directly affect the other. Some regional cirrus models are size resolving and allow direct coupling of the microphysical processes and radiative properties (Jensen et al. 1994a,b) but these are practical today only for certain temporally and spatially limited applications. The bulk water cloud parameterization and bulk optical properties will be the primary schemes used in GCMs and operational models for the near future; hence, these methods are employed in this paper. This simulation can then be used as a benchmark for future numerical studies wherein the bulk water microphysical parameterization and the optical properties are internally consistent.

1) Extinction

For ice clouds, it is difficult to find a simple relationship between ice water content (IWC) and extinction since ice crystals range from 10 μm to greater than 1 mm in length, their shapes are irregular, and they are sometimes hollow. Ebert and Curry's (1992) approximation to ice extinction β_{eS} (in km^{-1}) at all solar wavelengths,

$$\beta_{eS} = 10^3 \mathrm{IWC}(a_0 + b_0/r_e), \quad (1)$$

is used, where IWC has units of g m^{-3} and r_e has units of μm. The coefficients a_0 and b_0 equal 0.00413 and 2.92, respectively, and are based on the analysis of FIRE data by Kinne et al. (1996). For a given IWC, these constants provide 20% larger extinction than that predicted by Ebert and Curry, whose assumed particle density of 0.85 g cm^{-3} seems too high for the ice crystals observed during FIRE. The infrared extinction should be almost identical for the larger ice crystals. However, to compensate for the large infrared extinctions by smaller ice crystal sizes, a correction is introduced, based on calculations of the ratio of infrared window extinction to solar extinction for different ice crystal sizes

$$\beta_{e\mathrm{IR}} = \beta_{eS}(1.03 + 2.73/r_e). \quad (2)$$

The optical properties of liquid clouds must also be approximated since stratus occur at COF and other locations during the simulation. The relationship between liquid water content LWC and β_{eS} is based on the geometric optics approximation with an extinction cross section of 2. The extinction becomes

$$\beta_e = \frac{3 \times 10^3 \mathrm{LWC}}{2\rho r_e}, \quad (3)$$

where LWC has units of g m^{-3}. While this approximation is valid only for solar wavelengths, it is adopted for infrared wavelengths since the results compare favorably to explicit size-resolving infrared calculations. Large discrepancies for wavelengths beyond 20 μm are acceptable due to the reduced importance of that part of the spectrum for the cloud temperatures of this study.

2) Single scattering albedo

For both ice and water clouds, and at all wavelengths, Sagan and Pollack's (1967) estimate of the single-scattering albedo ω_0,

$$\omega_0 = 0.5 + 0.5 \exp(-2k_\lambda r_e), \quad (4)$$

is used, where $k_\lambda = 4\pi n_i/\lambda$ and the wavelength-dependent imaginary refractive index n_i is taken from Palmer and Williams (1974), Downing and Williams (1975), and Painter et al. (1969) for water clouds, and from Warren (1984) for ice clouds. This relationship is based on the geometrical optics approximation, the assumption that the cloud particle size is significantly larger than the wavelength. However, for longer infrared wavelengths, explicit size-resolving calculations show that this relationship still holds, except for the energetically less important far-infrared region (wavelengths greater than 15 μm). In fact, for the determination of the important absorption and emission processes, the error from the overestimation of ω_0 is partly compensated by the overestimation of β_e so that the absorption $\beta_a = [\beta_e(1 - \omega_0)]$ compares favorably with explicit calculations.

3) Asymmetry parameter

To accurately account for solar scattering of ice crystals, the Ebert and Curry (1992) approximation of the asymmetry parameter g,

$$g = e_i + f_i r_e, \quad (5)$$

is used. Their fit for the solar and near-IR wavelengths is based on geometrical optics calculations for hexagonal ice crystals by Takano and Liou (1989).

For water clouds at solar wavelengths, Sun and Shine's approximation for g,

$$g = e_w(\mathrm{LWC})^{f_w}, \quad (6)$$

is used. The coefficients e_w and f_w for 24 wavelength intervals are given in Sun and Shine (1994). For thermal wavelengths, scattering is less important since the absorption $(1 - \omega_0)$ is a significant fraction and therefore the nonsphericity of the crystals is neglected. Under these conditions, the importance of an accurate g is reduced. For cloud and ice, g is set to 0.87 and 0.9, respectively. The ice value of 0.9 allows for absorption which can be significant, particularly when large ice-crystals are present, as was the case during FIRE-II. It differs from the range of 0.7 to 0.75 determined by Stackhouse and Stephens (1991) since they considered only conservative scattering.

4) Effective particle radius

The use of Eqs. (1)–(5) requires the effective particle radius r_e. In the absence of an explicit prediction of r_e (e.g., Jensen et al. 1994a,b), r_e must be specified or parameterized in terms of predicted variables. For water cloud, r_e is set to 10 μm.

The aircraft and ice replicator sonde data from FIRE-II (Heymsfield et al. 1990) and FIRE-II (Heymsfield and Miloshevich 1995) are utilized to develop an expression for r_e for ice. In the analysis of these data, Kinne et al. (1992, 1996) make a number of assumptions about the probe characteristics and particle morphology. To predict the scattering by complex ice crystals, they break particles with associated cross sections larger than those expected for hexagonal columns (e.g., Heymsfield 1975) into fragments with hexagonal column shapes. To conserve extinction, each column is converted into a surface area-equivalent sphere, and the effective particle radius of the resulting distribution of spheres is captured by r_e. Scattering on hexagonal columns is quite different from that on equivalent spheres. However, the differences are known, at least at solar wavelengths, and parameterizations such as that by Ebert and Curry can be applied. The variability of r_e in the FIRE-I and FIRE-II data shown in Fig. 4 is typical and illustrates that r_e is not a simple function of temperature (T) or IWC. The two linear relationships shown in Figs. 4a and 4b are poor fits to the observations. A better approximation is possible if both T and IWC are included. For temperatures T warmer than -50°C and IWC greater than 10^{-4} g m^{-3}, r_e (in μm) is parameterized with

$$r_e = 30 + 1.2(50 + T)[4 + \log(\mathrm{IWC})]; \quad (7)$$

otherwise, it is 30 μm; r_e is further constrained to be less than 130 μm.

5) Sample radiative calculations

A practical example of the heating rates and surface fluxes calculated with the radiative transfer model using the bulk optical properties described above is shown in Fig. 5 and compared with those obtained from a two-stream size-resolving radiation model that explicitly calculates optical properties for ice crystal size distributions based on Mie theory and includes corrections for irregularly shaped particles (Kinne et al. 1996). Though differences in the spectral resolution and solution techniques used in the two radiative transfer models may also be a source of differences, calculations show that these are small compared with the error associated with the approximation to r_e and the prediction of IWC.

The temperature and relative humidity profiles used in the calculations are specified using the 2025 UTC COF sounding. The profile of ice crystal size distribution was derived from the 60-km long, constant-altitude NCAR Sabreliner and King Air flight legs during 1941–2046 UTC (Heymsfield and Miloshevich 1995; Kinne et al. 1996). The approximately 300-m vertical resolution data (dotted curves in Fig. 5) reveal multilayered cirrus between 6 and 9.5 km with a peak concentration of 45 mg m^{-3} at 8.2 km (Fig. 5a). The effective particle radius r_e is 74 μm near cloud base and decreases with altitude to 37 μm at cloud top (Fig. 5b). These profiles are undoubtedly dependent on the aircraft altitude and the averaging times but nevertheless have the characteristics of midlatitude cirrus.

The maxima of the longwave heating rates for the explicit size-resolving calculations with the 300-m resolution data are -12 K day^{-1} at cloud top and 8 K day^{-1} at cloud base (Fig. 5d). There is a second local maxima in the longwave heating rates at 8.2 km, the top of the densest cloud layer. The shortwave heating profile also reflects the layered structure (Fig. 5e). Maximum heating rates are 5.5 K day^{-1}.

To show the effect of coarse vertical resolution, the original 300-m resolution profiles are interpolated to the dynamical grid (approximately 700-m resolution), and another calculation is made with the size-resolving radiation code. Interpolation eliminates the layered structure of the cirrus and generates smoothed profiles of longwave cooling with maximum cooling of -11 K day^{-1} at midcloud and heating of 7 K day^{-1} at cloud base. The shortwave heating profile is also smoothed and maximum heating rates are 4 K day^{-1}.

The simplified model used in the 3D model differs from the size-resolving model by the use of bulk optical properties [e.g., Eqs. (1)–(6)] and the approximation of the explicit size distribution with r_e [Eq. (7)]. The effects of these two differences are looked at sepa-

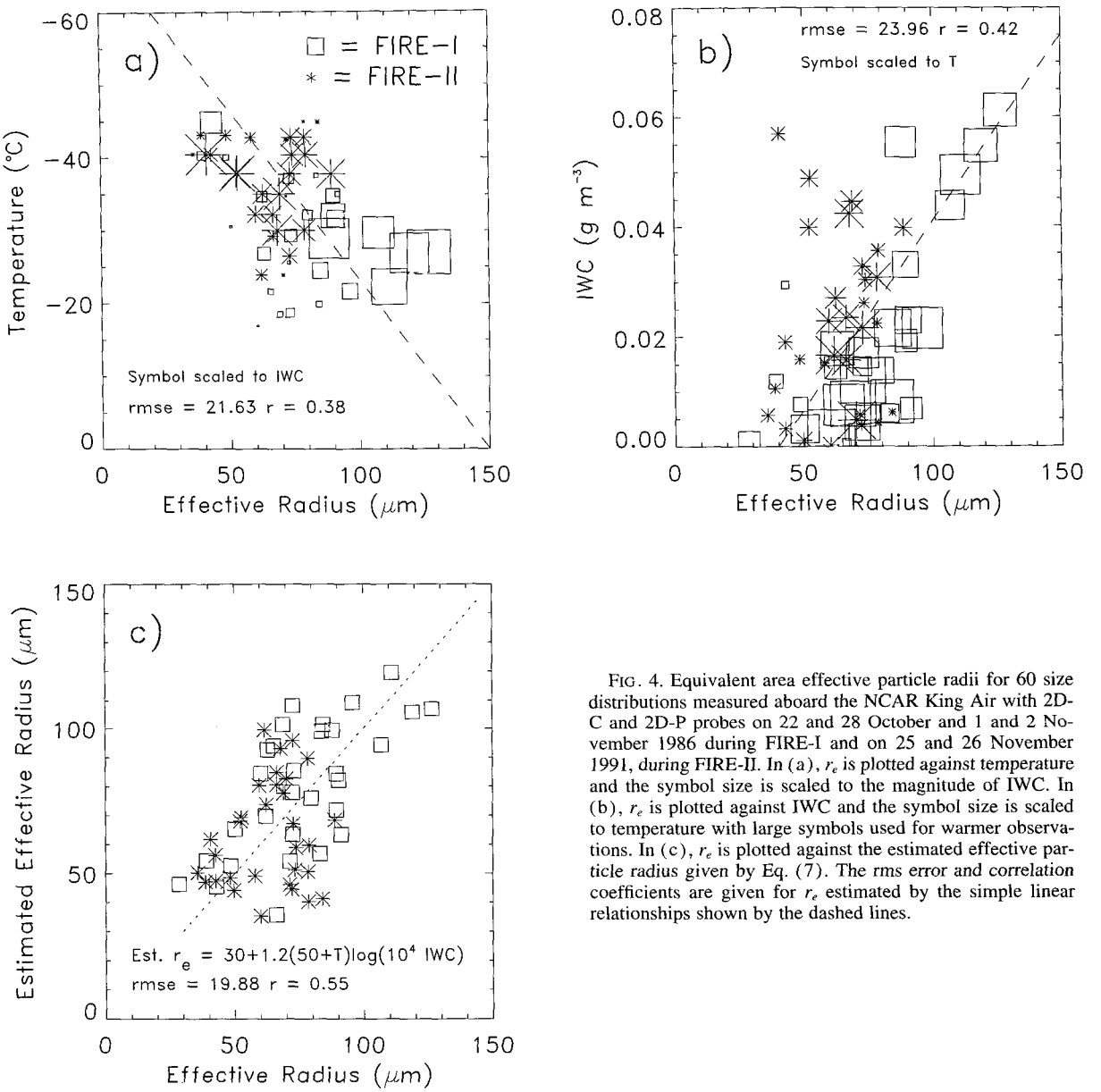

FIG. 4. Equivalent area effective particle radii for 60 size distributions measured aboard the NCAR King Air with 2D-C and 2D-P probes on 22 and 28 October and 1 and 2 November 1986 during FIRE-I and on 25 and 26 November 1991, during FIRE-II. In (a), r_e is plotted against temperature and the symbol size is scaled to the magnitude of IWC. In (b), r_e is plotted against IWC and the symbol size is scaled to temperature with large symbols used for warmer observations. In (c), r_e is plotted against the estimated effective particle radius given by Eq. (7). The rms error and correlation coefficients are given for r_e estimated by the simple linear relationships shown by the dashed lines.

rately. First, the adequacy of the bulk optical properties is demonstrated by using the exact profiles of IWC and r_e that were explicitly calculated from the aircraft data by Kinne et al. (1995). Figure 5c shows that Eq. (1) yields β_{eS} within a few percent of the 700-m values. The resulting cloud-top longwave cooling and solar heating are within 20% of the 700-m values (Figs. 5d–f) and reflect the accuracy of this approximation to the optical properties.

The effect of the approximation for r_e is shown in a second simplified calculation that uses the same profile of IWC but now r_e is defined by Eq. (7) using the observed IWC and T. Equation (7) yields a slightly lower r_e at cloud top but overestimates r_e by up to 40% at midcloud and cloud base. [A different approximation for r_e might seem warranted, but Fig. 4 shows that Eq. (7) underestimates r_e for other cases.] This leads to a slight overestimate of β_e at cloud top and an underestimate of β_e at cloud base owing to its inverse dependence on r_e. Thus, the magnitude of the longwave cloud-top cooling is slightly higher and the cloud-base warming is reasonable, but the peak cooling rate at midcloud is underestimated by 40%.

The boundary radiative fluxes from these different cases are compared in Table 1. There are only small differences between the two size-resolving calculations and the simplified calculation that used the observed r_e. The albedos are nearly identical to that inferred from

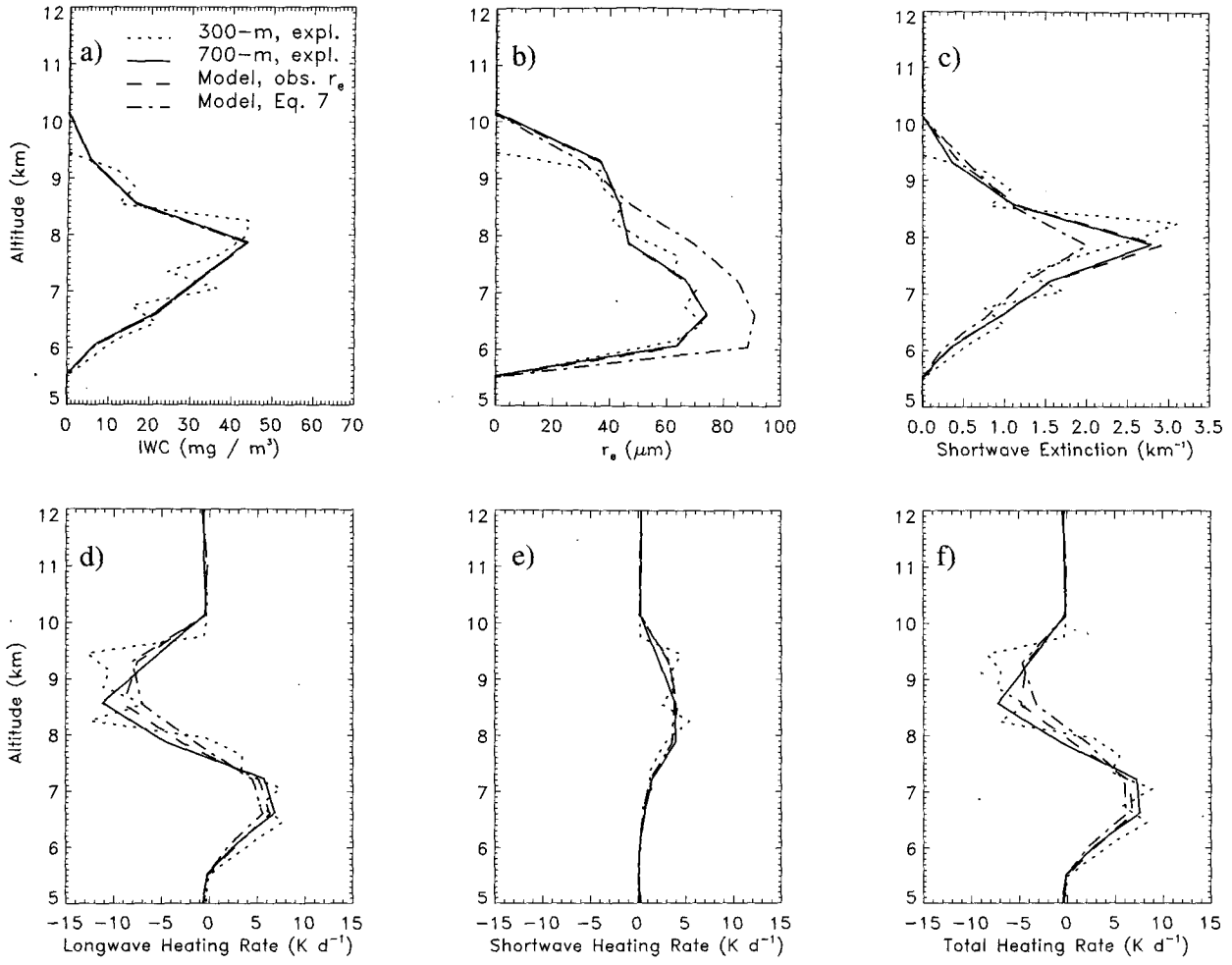

FIG. 5. Vertical profiles for COF at approximately 2030 UTC of (a) IWC (mg m^{-3}); (b) r_e (μm); (c) shortwave β_e (km^{-1}); (d) longwave heating rate; (e) shortwave heating rate; and (f) total radiative heating rate. Four cases are shown. Solid line: size-resolving radiation model with 700-m resolution; dotted line: size-resolving radiation model with 300-m resolution; dashed line: simplified model with 700-m data and using observed IWC and r_e; dot-dash line: simplified model with 700-m data and using observed IWC and r_e from Eq. (7); T and RH_i are taken from the 2025 UTC COF sounding. IWC and r_e profiles are calculated from the NCAR aircraft data from 1941 to 2047 UTC except for the dot–dash line in (b), which is given by Eq. (7) using the observed T and IWC.

Geostationary Orbiting Environmental Satellite (GOES) imagery by Minnis et al. (1993). When Eq. (7) is used for r_e, it underestimates β_{eS} causing the solar albedo to be underestimated and the surface solar flux to be overestimated. The longwave surface fluxes for all four cases are similar. The upward longwave fluxes at model top calculated with the simplified model are 5 W m^{-2} lower due to the slightly higher values of β_{eIR} near cloud top. The "simulation" entries in the table are discussed in section 7.

3. Case study description

The focus of this paper is the second of three Intensive Observation Periods (IOP) during FIRE-II, which began at 1500 UTC 25 November and ended 36 hours later at 0000 UTC 27 November. The scope of the paper is further reduced to 0000 UTC 26 November through 0000 UTC 27 November since there was a progression from clear skies to cirrus and then to altocumulus at COF during which multiple in situ missions were flown and nearly all of the surface instrumentation was operational. In this discussion, the "IOP area" is defined as the region within 200 km of COF.

At 0000 UTC the IOP area was cloud free after the passage of a trough on 25 November (Figs. 1a and 3a). By 1200 UTC a shortwave moved into the Wyoming–Nebraska area, and a split-flow pattern existed over the central plains with diffluent flow over Oklahoma and Kansas (Figure 6a). Except for a small patch of cirrus at 0900 UTC, the IOP area remained clear. A large-scale ridge and jet streak was situated over the Rocky Mountains. During the next 12 h, the shortwave trough moved southeastward so that by 0000 UTC 27 Novem-

TABLE 1. Calculated top-of-atmosphere and surface radiative properties for COF. Fluxes are in watts per square meter; albedo A is unitless. All cases assume 2100 UTC and use a solar zenith angle $u_0 = 0.35$ except as noted.

	Radiative property				
	Top of atmosphere			Surface	
Calculation	S↑	A	L↑	S↓	L↓
Explicit size-resolving model:					
700-m resolution	258	54	161	171	316
300-m resolution	260	54	158	168	316
Simplified model:					
using observed IWC and r_e	252	55	151	169	316
using observed IWC but r_e from Eq. (7)	237	52	153	185	314
simulation of 20 UTC ($u_0 = 0.46$)	354	59	128	199	294
simulation at 21 UTC	294	63	132	125	300
GOES (Minnis et al. 1993):					
analysis at 21 UTC		54			

ber it coincided with the axis of the large-scale trough situated directly over COF (Fig. 6b). A jet streak was entering Kansas. Mace et al. (1995) have shown that the eastward movement of this shortwave and jet streak resulted in moderate upward motions and cloud formation in the IOP region beginning around 1700 UTC. This cloud field was intensively observed during the second FIRE-II IOP and will hereafter be called the "IOP cloud field." By 0000 UTC 27 November, the IOP region began to clear (Fig. 1c) due to the strong sinking flow associated with the approaching large-scale ridge (Fig. 6b).

4. Dynamics validation

The validity of using the MM4 model for developing cloud parameterizations and comparing the predictions to observations depends upon the ability of the model to simulate the dynamical forcing. This section is devoted to a comparison of the simulation with NMC analyses, rawinsonde data, and wind profiler data.

The simulated 300-hPa heights and winds at 1200, 1800, and 2100 UTC are compared with the rawinsonde and wind profiler data in Figs. 3b–d. These times correspond to 12, 18, and 21 h into the simulation. The agreement between the observations and the simulation is excellent at 1200 and 1800 UTC, but at 2100 UTC the simulated jet streak lags the observations by 100 km. This lag is better illustrated by comparing in Fig. 7 the simulated time section of wind speed and direction with that analyzed by Mace et al. (1995) using the wind profiler from Neodesha, Kansas (NDS in Fig. 2), some 50 km north of COF. The model simulates the general features of the observed wind field, including the strong southerly low-level flow for most of the day and the gradual decrease in the southerly wind component in the mid and upper troposphere. The 250-hPa jet, as denoted by the 25 m s^{-1} isotach, reaches NDS at 1600 UTC and is gone by 2200 UTC, while the simulation has the jet passing over NDS two hours later. At about 2300 UTC, the observed trough passes NDS and the 9-km winds take on a northerly component. However, even by 0000 UTC 27 November the simulated trough has not passed and the winds still have a southerly component.

As discussed by Mace et al. (1995), the upward motions at NDS between 1800 UTC 26 November and 0000 UTC 27 November are induced by the shortwave and approaching jet. In their time-series analysis (Fig. 8a), vertical velocities greater than 6 cm s^{-1} are found at 5 km between 1920 and 2025 UTC and then again at 3.5 km between 2140 and 2310 UTC. The time section of simulated vertical velocity at COF (Fig. 8b) shows similar magnitudes and timing, but the maxima occurs 2 km higher and does not move to lower levels, instead staying centered at 7 km. Strong positive motions in the middle and upper troposphere are still present at 0000 UTC 27 November.

The differences between the simulated and analyzed timing of the trough passage and the three-dimensional wind fields will cause errors in the simulation of the IOP cloud field and must be kept in mind during the following comparisons between observations and the simulated cloud and radiation fields. For example, in comparison to the observations, the simulated clouds are expected to linger at COF due to the delayed arrival of the ridge and jet and the persistence of strong upward motions. This is discussed further below.

5. Water vapor validation

In addition to an accurate dynamical simulation, the cloud simulation depends heavily on the initial water vapor distribution. The initial conditions are discussed in the next subsection and are followed by verification of the regional moisture distribution and then a verification of the distribution at COF. For the discussion, the use of a conserved moisture variable such as virtual

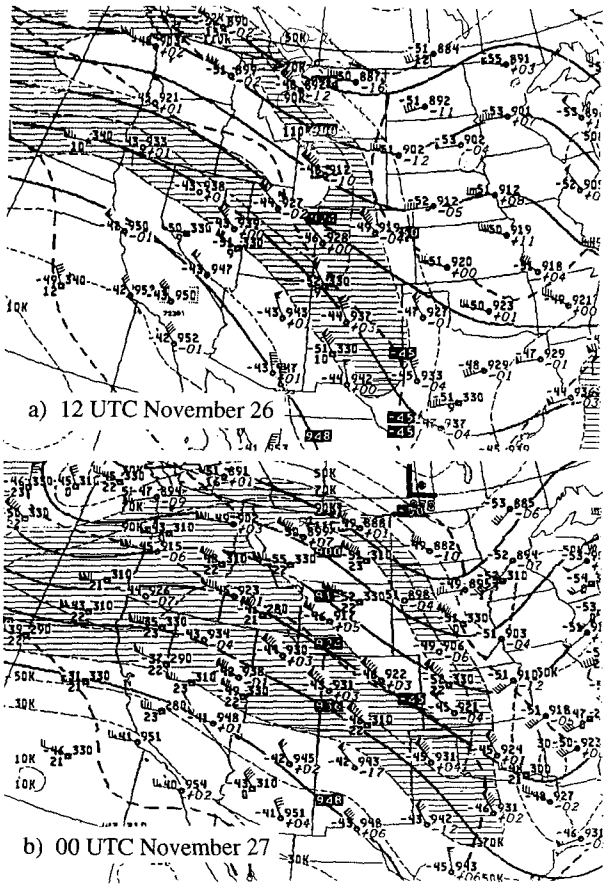

FIG. 6. The NMC analyses of the 300-hPa geopotential height (solid lines, contour interval of 12 dm), isotachs (thin-dashed lines, contour interval of 20 kt; the region with wind between 70 and 110 kn is hatched), and temperature (thick solid lines, contour interval of 5 K) for 1200 UTC 26 November and 0000 UTC 27 November.

potential temperature is often desirable, but the moisture layers where cirrus form are not easily detected with that variable due to the low temperatures, mixing ratios, and pressures. Instead, this discussion utilizes analyses of relative humidity with respect to ice RH_i from rawinsonde and Raman lidar (Ferrare et al. 1992) and the mean upper-tropospheric humidity (UTH_{GOES}) inferred from GOES (Soden and Bretherton 1993). The Raman lidar mixing ratios are converted to RH_i using the CLASS temperature profiles. Relative humidity better illustrates the horizontal and vertical variability of the potential for cirrus cloud formation. Though the cloud simulation is discussed in a later section, it is convenient to present some of the cloud observations in this section.

a. Initial conditions

Animation of the infrared GOES imagery, along with the simulated back trajectories presented in Fig. 9, shows that the air mass containing the IOP cloud field originated between Oregon and Colorado at 0000 UTC. The water vapor distribution must be accurately known over this region at the initial time in order to accurately simulate the cirrus during the IOP. As stated previously, FIRE-II chose to fulfill this requirement by relying on enhanced NWS rawinsonde releases and working with the staff at NWS and NOAA to assure that these asynoptic soundings were transmitted over Automation of Field of Operations and Services (AFOS) and assimilated by MAPS. Here, the available observations and analyses of moisture upwind of COF at the initial time are presented and compared.

A quantitative estimate of the mean upper-tropospheric relative humidity UTH_{GOES} has been derived by Soden et al. (1994) from the GOES 6.7-μm radiances and is shown in Fig. 10a. Their method yields a synoptic view of the distribution of mean upper-tropospheric relative humidity UTH_{GOES} in cloud-free regions at hourly intervals during the second IOP. In addition to high humidity covering Nevada, Idaho, and Wyoming at 0000 UTC, their analysis reveals two ex-

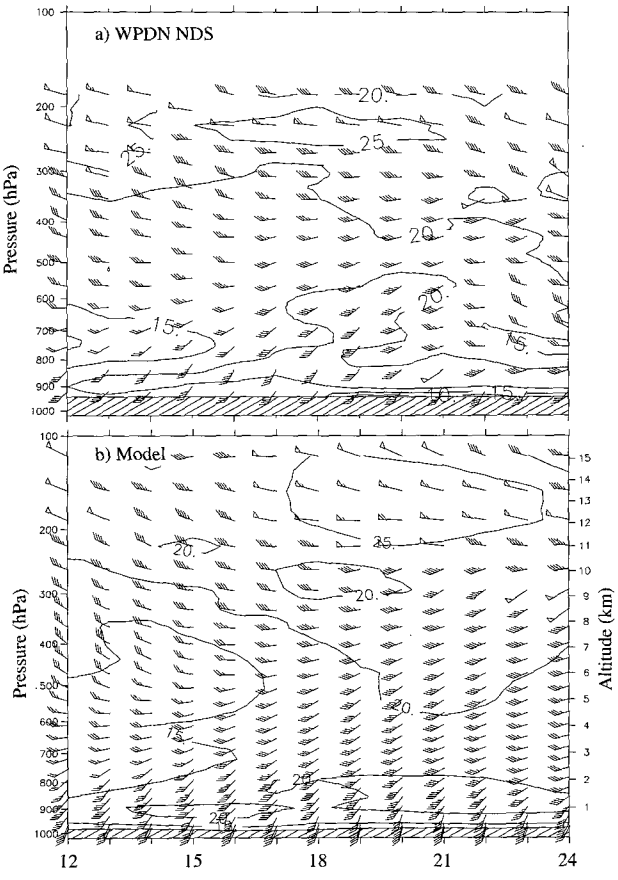

FIG. 7. Time sections for 1200 UTC 26 November–0000 UTC 27 November at NDS of wind speed and direction (full barbs equal 5 m s^{-1}; each flag equals 25 m s^{-1}) and wind speed (contour interval of 5 m s^{-1}) derived from (a) NOAA WPDN data analyzed by Mace et al. (1995) and (b) simulation.

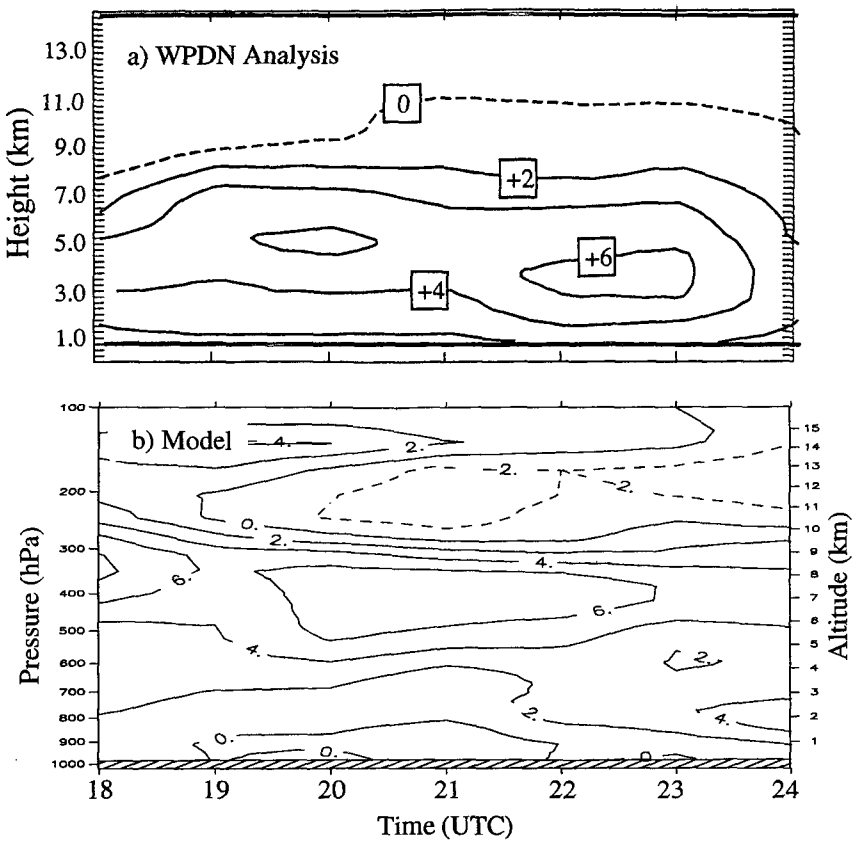

FIG. 8. Time section of vertical wind speed (contour interval of 2 cm s^{-1}) at COF for 1800 UTC 26 November–0000 UTC 27 November (a) diagnosed from WPDN data by Mace et al. (1995) and (b) simulated. Negative contours are dashed.

tensive meridional features of high UTH_{GOES} reaching southward through Utah into Arizona and through Colorado into New Mexico. Animation of the images reveals that these features propagate eastward during the period and therefore are not artifacts of mountainous regions. The origins of the 18-h and 21-h back trajectories are marked in Fig. 10. Some trajectories originate along the axis of high-UTH_{GOES} feature in Colorado and in the moist Pacific Northwest, while others originate in the adjacent dry regions. It is clear that the atmospheric column that was probed at COF during the last hours of the IOP originated over a large area with a wide range of initial humidities.

Because of their wide spacing, the rawinsondes cannot adequately describe the fine horizontal structure of the humidity field. This is shown in Figs. 11a and 12a with vertical cross sections of RH_i in the vicinity of the origins of the 18-h and 21-h trajectories using data from Amarillo, Texas (AMA); Boise, Idaho (BOI); Denver, Colorado (DEN); Grand Junction, Colorado (GJT); Lander, Wyoming (LND); Salem, Oregon (SLE); Salt Lake City, Utah (SLC); and Stephenville, Texas (SEP). The cross sections use the NWS Microcomputer Automated Radio Theodolite (Micro-ART) 6-s data, as processed by D. Starr (1994, personal communication) and corrected as described by D. Westphal (1996, manuscript submitted to *J. Atmos. Oceanic Technol.*). The corrections are largest for the Space Data Division (SDD) rawinsondes (denoted by triangles in Fig. 9) and at RH_i extremes and cold temperatures. The cross section of the uncorrected data (not shown) had unusually high values of RH_i well above the tropopause, while in the corrected cross section, RH_i is reduced by 20% at LND, though the stratospheric values are probably still too high, perhaps due to other uncorrectable biases described by Westphal.

In agreement with the UTH_{GOES} analysis, the NWS data (Figs. 11a and 12a) show moist conditions in the west and very dry conditions at AMA. This is also in agreement with surface reports of multilevel clouds at all stations and only cirrus wisps at AMA. The lack of a moist layer aloft at DEN is unexpected since DEN lies near the axis of the meridional feature of high UTH_{GOES} (Fig. 10a). There is no evidence of this moist layer in the SLE–SEP cross section since GJT and AMA lie to either side of it. The rawinsonde data clearly do not resolve the horizontal and vertical distribution of moisture over the range of back trajectory

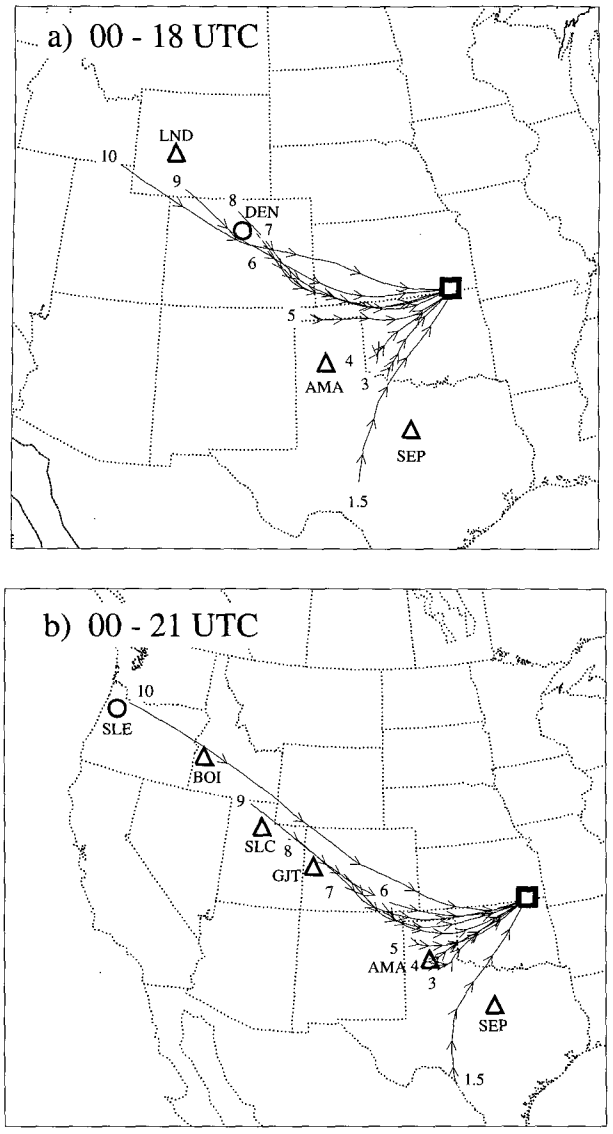

FIG. 9. Simulated 18-h and 21-h back trajectories for parcels terminating at (a) 1800 UTC and (b) 2100 UTC over COF at altitudes of 3–10 km at 1-km intervals and at 1.5 km. Each trajectory is labeled with the final altitude of each parcel arriving at COF. The arrowheads mark the movement over a 3-h period. Rawinsonde stations used in cross sections shown in Figs. 11 and 12 are labeled for reference.

origins. There are no other data that adequately determine the vertical distribution of water vapor at the scales employed by the dynamical model. These rawinsondes were the only source of moisture data above the surface for the MAPS data assimilation cycle.

The MAPS analyses are verified by calculating a mass-weighted, average relative humidity UTH_{MAPS} for the 200–500 hPa (~6–11 km) region of the atmosphere and comparing this with UTH_{GOES} in Fig. 10. Soden and Bretherton (1993) show that this simple averaging of observed or modeled data is adequate for comparing with UTH_{GOES} even though the weighting function for the 6.7-μm channel is not constant in the layer. The distribution of UTH_{MAPS} shown in Fig. 10b duplicates the general features of high UTH_{GOES} over the intermountain region and Arkansas and a dry tongue from southwest Minnesota to the Texas panhandle, but the values of UTH_{MAPS} are generally lower than UTH_{GOES} everywhere, the features are not as sharply defined, and the two meridional features of high humidity are missing. The MAPS analysis places an area of high UTH_{GOES} in western Colorado and gives it a northwest–southeast tilt. As a result, the 18-h 6-km through 9-km back trajectories and the 21-h 6-km back trajectory originate in a region of UTH_{MAPS} less than 35%, or less than one half the values of UTH_{GOES}.

The presence of cloud, which prevents Soden et al. (1994) from analyzing UTH_{GOES} in a particular region, does not necessarily imply high UTH since only a single thin cloud layer may be sufficient to saturate the 6.7-μm channel even when the actual mean relative humidity is low. Thus, the comparison of UTH_{GOES} and UTH_{MAPS} cannot not be done in the cloudy regions of Idaho, Wyoming, and Oregon. However, the surface reports from stations in those states include widespread observations of multiple cloud layers and precipitation prompting the conclusion that the troposphere is moist at more than a single shallow layer over much of these states.

The general trend of low UTH_{MAPS}, compared to UTH_{GOES}, can be explained by comparison of the MAPS and NWS cross sections along the trajectory origins (Figs. 11 and 12). MAPS correctly analyzes the general low- and midlevel RH features of both NWS cross sections but shows a lack or underestimation of the upper-level RH_i maxima above the −40°C isotherm. This general characteristic of the MAPS data is due to the NWS convention of deleting RH data at these temperatures before transmission over AFOS. No moisture data are available to MAPS at temperatures less than −40°C. As a result, the RH_i at the origins of the 18-h 8-km and 9-km back trajectories and the 21-h 10-km back trajectory are less than 10% and only a fraction of the NWS tropospheric values. In the next section, the dynamical model is shown to generate a reasonable moisture distribution from this initially dry state. The MAPS forecast cycle is expected to also have produced a better moisture distribution, but the 12-h forecast fields are unavailable for comparison.

b. Regional simulation

The IOP cloud field appears both in the 2200 UTC infrared satellite imagery (Fig. 1b) and in the distribution of UTH_{GOES} at 2100 UTC (Fig. 13a) as clouds and high humidity running SSW from the upper Mississippi Valley to Oklahoma and southward into Texas. Clouds or high UTH associated with the large-scale ridge in the west occupy all of the Pacific Northwest

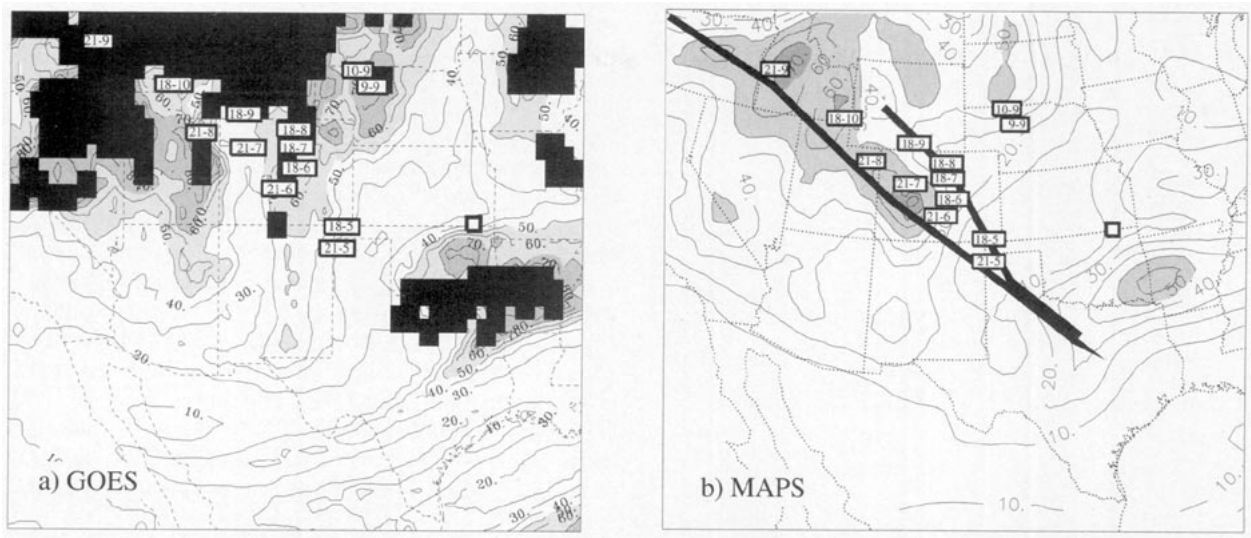

FIG. 10. Mean upper-tropospheric humidity with respect to water (contour interval of 10%) for 0000 UTC (a) derived by Soden et al. (1994) from GOES 6.7-μm data for cloud-free regions on a Mercator projection, and (b) mass-weighted mean of the MAPS RH data for the 200–500-hPa layer on a polar stereographic projection. Cloud-filled regions where the GOES analysis was not possible are shaded black. The approximate location of the origins of the 18-h and 21-h back trajectories (Fig. 9) are marked with the final altitude and hour as "hour-alt"; for example, 18-9 marks the origin of the parcel arriving at COF at 1800 UTC and an altitude of 9 km. The thick solid lines in (b) denote the location of the cross sections shown in Figs. 11 and 12. Also shown are the origins of the 0000–0900 UTC back trajectories.

and the intermountain west. The sinking air behind the shortwave and ahead of the ridge cause the two moist regions to be separated by a dry area running south from North Dakota to central Texas. The MAPS analysis of UTH at 2100 UTC (Fig. 13b) resolves the moisture feature in the upper Mississippi Valley and the IOP cloud field in Kansas but does not extend the moisture into Oklahoma or Texas. The values of high UTH over the intermountain west are absent except over Oregon.

The simulation of UTH at 2100 UTC (UTH_{Sim}; Fig. 13c) resolves the feature in the upper Mississippi Valley and the IOP cloud field, and it closely resembles the UTH_{GOES} analysis in that it is nearly as extensive, has sharp gradients on the west and east, and extends into Oklahoma and Texas. The western border of IOP cloud field and its southward extension into Texas is west of that in the GOES analyses, owing to the slower simulated progression of the shortwave. In the intermountain west, simulated areas of high UTH are distributed less extensively than in the GOES analysis but are much more extensive than in the MAPS analysis. The dry area between the cloud fields is simulated, though this feature is also just west of the observed location.

c. *Simulation at COF*

Several data sources are used to validate the simulated water vapor profile at COF. NWS and NCAR CLASS rawinsonde data and Raman lidar data are used directly. Observations of cloud boundaries by lidar and radar are used to imply conditions of saturation with respect to ice. The NOAA/Environmental Technology Laboratory's (ETL) radiometers located at COF yield a continuous estimate of precipitable water and indicate the presence of clouds.

The COF CLASS rawinsonde data shown in Fig. 14a indicate that the mid- and upper troposphere are generally dry during 0000–1200 UTC. However, the NOAA radar and lidar (Fig. 15), and the Langley Research Center's lidar at Parsons, Kansas (PAR), detected clouds at levels from 6.5 to 10.4 km between 0900 and 1100 UTC. The nominal frequency of the CLASS rawinsonde releases is insufficient to resolve the moist upper-tropospheric conditions associated with these cirrus clouds. However, the Goddard Space Flight Center's (GSFC) Raman lidar data (Ferrare et al. 1992) for 0000–1200 UTC has been combined with the NCAR CLASS data in Fig. 14b to produce an analysis that does show upper-tropospheric moistening beginning at 0300 UTC with the deepest moist layer occurring at the time the cirrus were observed. The Raman data are available only up to an altitude of 10 km and until 1200 UTC, but moistening likely extends to higher altitudes and later into the day since the lidars detected cirrus up to the tropopause at 10.6 km at 1300 UTC (Fig. 15). Back-trajectory analysis and the animation of satellite imagery and the UTH_{GOES} analyses reveal this moisture feature as originating north of North Platte, Nebraska (LBF), at 0000 UTC (Figs. 1a and 10a) and slowly dissipating as it moves SSE ahead of the IOP cloud field. This feature was not present in the initial conditions (Fig. 10b) and was not simulated by the model (Fig. 14e).

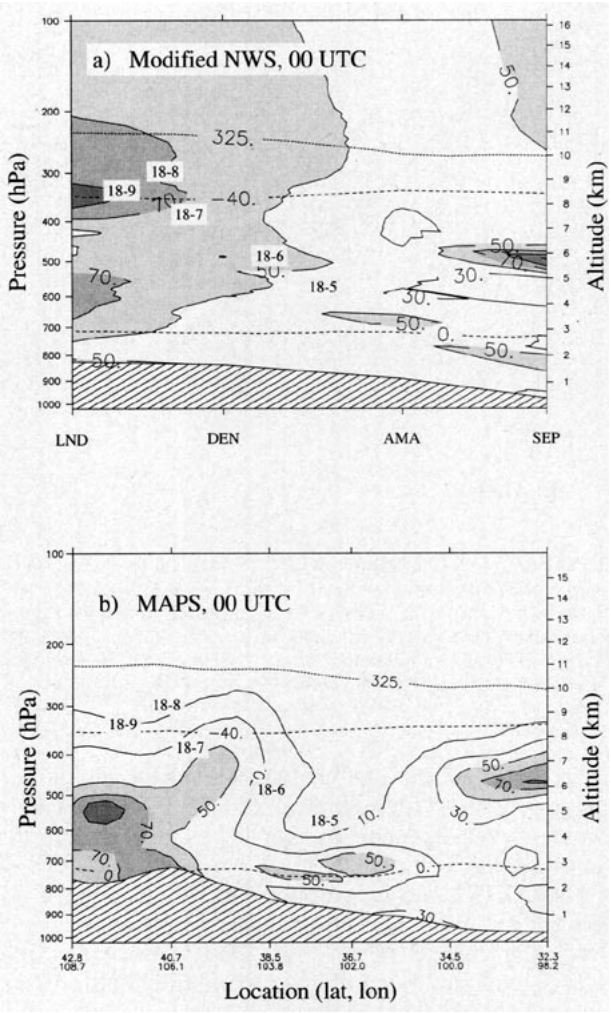

FIG. 11. Cross sections of relative humidity with respect to ice from Lander, Wyoming (LND), to Stephenville, Texas (SEP) (shorter solid line in Fig. 10b). This line corresponds to the approximate origins of the 18-h trajectories shown in Fig. 9a; RH_i is contoured with solid lines every 10% and also shaded for RH_i greater than 50%. Here, RH is with respect to water at temperatures above 0°C. All stations except Denver, Colorado (DEN), use SDD sondes. (a) Corrected NWS rawinsonde data (Westphal 1996). (b) MAPS analyses. The approximate location of the origins of the 18-h back trajectories are annotated as in Fig. 10. The 325-K contour of potential temperature is marked and is roughly the potential temperature of the tropopause on this day. Also shown is the −40°C contour of temperature, above which NWS rawinsonde humidity data were not routinely transmitted nor utilized in the MAPS assimilation system.

The precipitable water amounts detected by the NOAA/ETL microwave radiometer and integrated from NCAR/CLASS sondes (Fig. 16) show general agreement with amounts of less than 2 cm for the entire period. The precipitable water doubles from 1200 to 2200 UTC as the IOP cloud field progresses across Kansas (Fig. 16). The hourly UTH_{GOES} analyses also show gradual upper-tropospheric moistening over the IOP region during this period, but the increase in precipitable water is due primarily to the moistening of the lower troposphere. During the first 16 h of the simulation, the simulated precipitable water at COF is only 60% to 70% of the observed amount. Comparison of Fig. 14c and 14e indicates that the low simulated precipitable water amounts are due to a dry simulated lower and middle troposphere. The simulated precipitable water increases during the last 12 h, but is always less than the observed amount.

The NOAA radar and lidar reported high cirrus between 10.1 and 10.6 km at 1337 UTC and midlevel cirrus between 6 and 7 km at 1440 and 1553 UTC (Fig. 15). The high layer is unresolved by both the 1415 UTC rawinsonde (Fig. 14a) and the 1200 and 1500 UTC MAPS analyses (Fig. 14d), but the simulation shows signs of increasing RH_i at these altitudes and times (Fig. 14e). The midlevel layer is detected by the

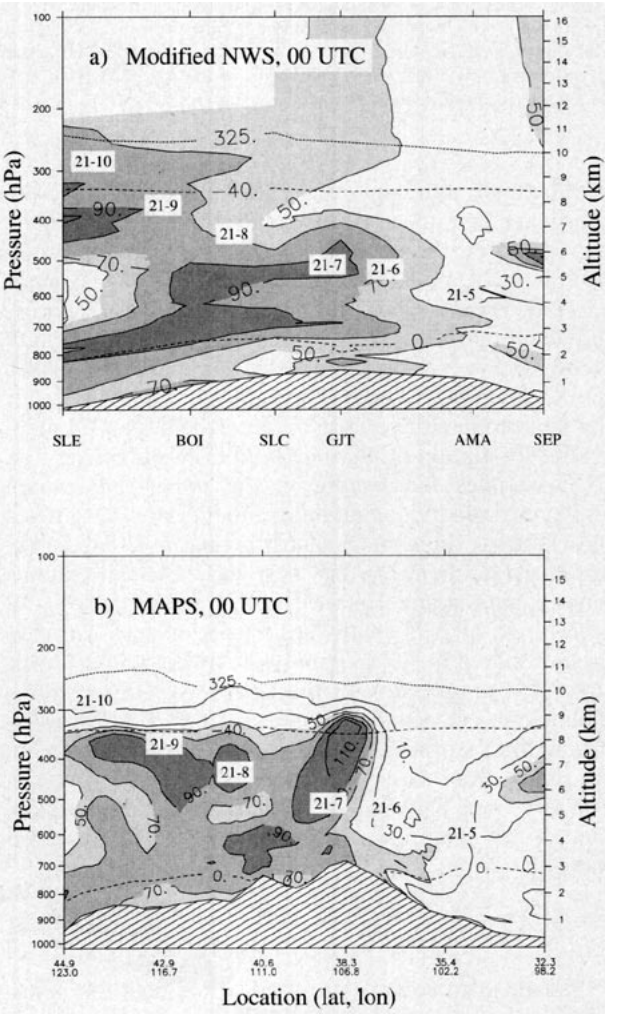

FIG. 12. As in Fig. 11 except from Salem, Oregon (SLE), to SEP, (longer solid line in Fig. 10b). This line corresponds to the approximate origins of the 21-h trajectories shown in Fig. 9b. All stations except SLE use SDD sondes.

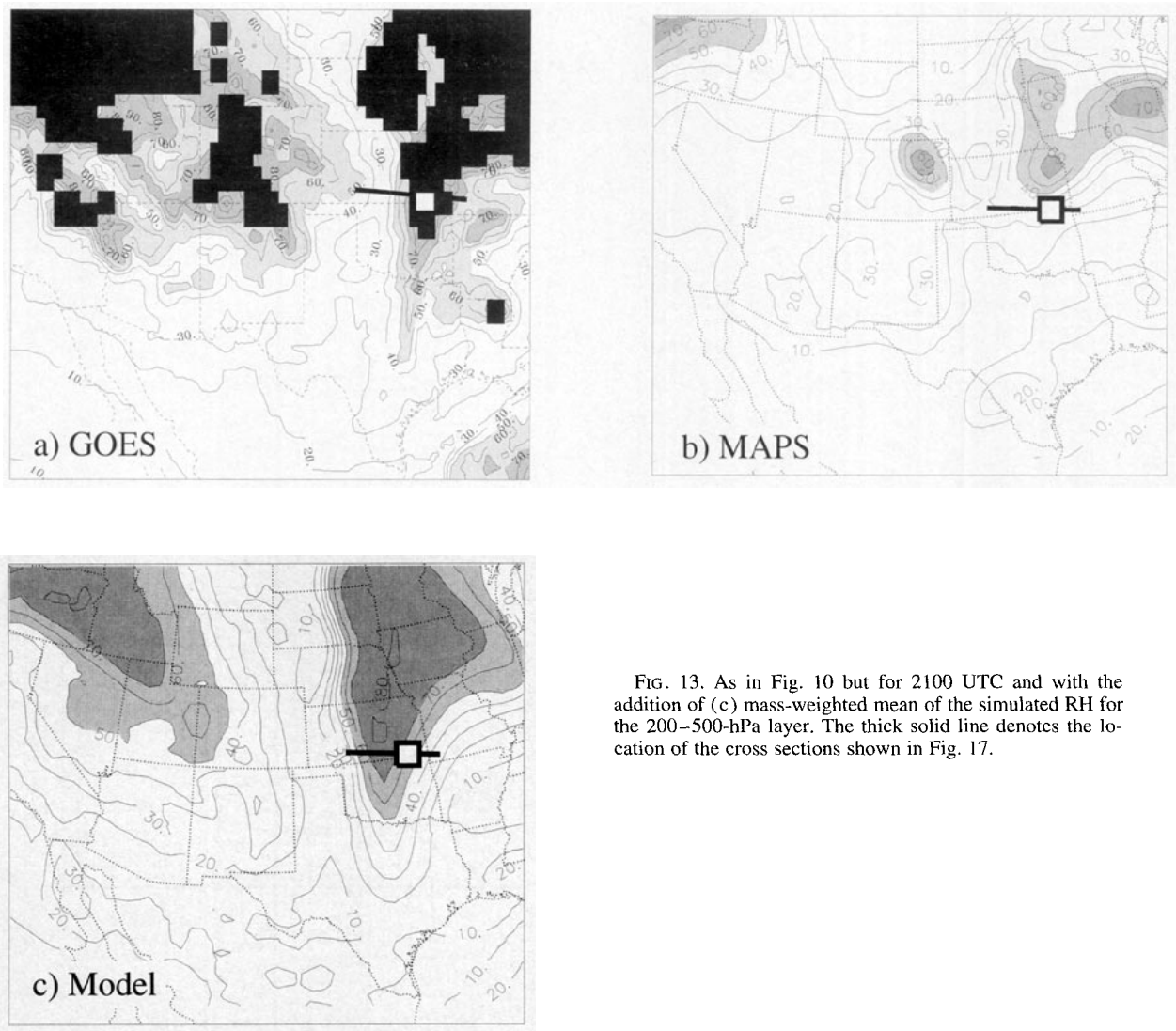

FIG. 13. As in Fig. 10 but for 2100 UTC and with the addition of (c) mass-weighted mean of the simulated RH for the 200–500-hPa layer. The thick solid line denotes the location of the cross sections shown in Fig. 17.

1415 UTC rawinsonde, appearing in Fig. 14a as the region of 70% RH_i at 7 km. This layer occurs at an altitude below the −40°C isotherm and is analyzed by MAPS, which shows RH_i greater than 70%. It appears only weakly in the simulation as a layer with RH_i between 30% and 50%.

The NOAA lidar shows the IOP cloud field arriving at 1646 UTC between 9.4 and 10.2 km (Fig. 15) followed by a trend of decreasing cloud-top heights through 0000 UTC 27 November, though there are some lidar returns from as high as the tropopause at 2100 and 2130 UTC. After that time, the cloud deepens, attenuation increases, and there are no more lidar or radar returns from above 9.7 km. The idea of a lowering cloud top is supported by the GOES analyses (Minnis et al. 1993), which show relatively warm brightness temperatures of 250 K (6-km altitude for a cloud with unity emissivity). However, these data do not exclude the possibility of a thin layer of near-tropopause cirrus after 2200 UTC. Kinne et al. (1992) found that during FIRE-I the physical cloud top was often 1 to 2 km above that detected by downward-looking broadband radiometers aboard the ER-2. There are no other direct observations to verify the cloud-top altitude during this time. The Sabreliner probably did not reach cloud top because there were intermittent counts for the Particle Measurement Systems's 2D-C probe at its highest altitude.

The 1716 and 2025 UTC rawinsondes detect only a slight moistening above 8 km to a RH_i of 50% (Fig. 14a). In contrast, the 2330 UTC sounding shows erroneously high values even into the stratosphere, a behavior typical of NWS rawinsondes. The continuous cloud field detected by lidar and radar during 1800–2300 UTC (Fig. 15) makes it unlikely that the 1716 or 2025 UTC soundings at COF passed through a clear

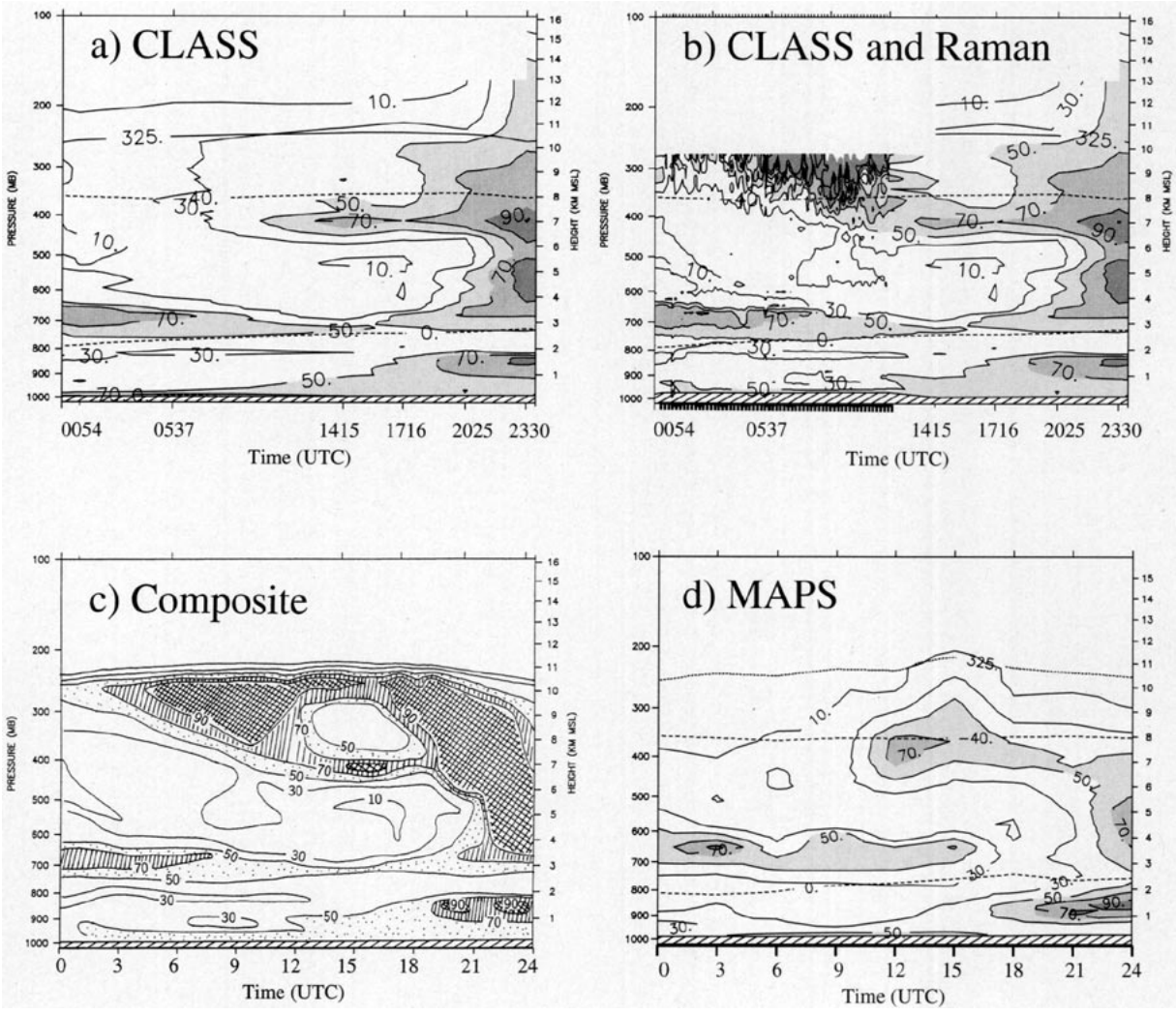

FIG. 14. Time section of relative humidity with respect to ice at COF for 0000 UTC 26 November–0000 UTC 27 November. Variables are presented with same conventions as in Fig. 11. (a) Analysis of COF NCAR CLASS data, (b) analysis of COF NCAR CLASS data plus Raman lidar data, (c) subjective composite of CLASS and Raman data plus inferences made from lidar and radar data, (d) MAPS analyses, and (e) simulation.

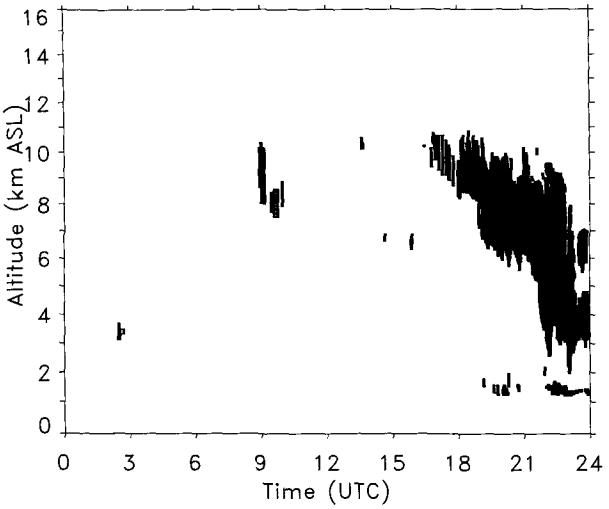

FIG. 15. Time history of the cloud boundaries at COF on 26 November as detected by NOAA radar and lidar (Uttal et al. 1995). Radar data are available for 1800–2400 UTC.

region during the ascent. Instead a dry bias in the CLASS humidity sensor is suspected.

The subjective analysis of RH_i shown in Fig. 14c was developed by combining the rawinsonde and Raman lidar data with inferences from the lidar, radar, and UTH_{GOES} data. It is assumed, conservatively, that the RH_i exceeds 90% wherever cirrus were detected by radar and lidar. The significant differences between this analysis and that derived from the COF soundings and Raman lidar are the nearly continuous region of high RH_i above 7 km during the period, and drier conditions above 7 km at 0000 UTC 27 November.

This moisture layer initially occurs at altitudes above the −40°C isotherm, and MAPS (Fig. 14d) resolves it only after it deepens and reaches temperatures warmer than −40°C. Though the model misses the moist layer prior to 1600 UTC, it accurately simulates the timing, altitude, and degree of the moistening after 1600 UTC (Fig. 14e). The simulated dynamical forcing is strong enough to saturate the atmosphere over COF in spite of the dry initial state. The details of the simulated IOP cloud field are discussed in section 6.

d. Simulation over the IOP region

The spatial extent of the moist layers observed at COF is apparent in the E–W cross sections of RH_i across the axis of the IOP cloud field at 2100 UTC shown in Fig. 17. Figure 17a shows the tendency of the VIZ Corporation (VIZ) sensors [Dodge City, Kansas (DDC), and Monett, Missouri (UMN)] to report high relative humidity in the stratosphere (D. Westphal 1996, manuscript submitted to *J. Atmos. Oceanic Technol.*), while the NCAR CLASS sondes [Arkansas City, Kansas (ARK), and COF] report more reasonable values. The high UTH values in the IOP cloud field are represented in the cross section as a deep moist layer at ARK and moderate RH_i at COF and UMN between 7 and 9 km. The radar data indicate that at 2100 UTC clouds were present at COF between 6 and 10 km. Furthermore, the analysis of GOES data by Minnis et al. (1993) shows that high, thin, cirrus were as far east as UMN (Figs. 18a and 18b). It is concluded that both the CLASS and NWS rawinsonde data underestimate RH_i in the upper troposphere at 2100 UTC. Additionally, both the UTH_{GOES} maxima located between ARK and COF and the minima between DDC and ARK (Fig. 13a) are unresolved in this cross section due to the spacing of the stations. These inferences and corrections are incorporated with the CLASS and NWS data to produce the composite of the cross section of RH_i shown in Fig. 17b. The changes include a sharpening of the gradient west of ARK, increasing the midtropospheric values between ARK and COF, and a deepening of the moist layer at COF and UMN.

As before, the MAPS analysis (Fig. 17c) shows a rapid decrease in RH_i at altitudes above the −40°C isotherm and thus does not resolve the IOP cloud field. The mid- and low-level moisture layers are resolved. The model (Fig. 17d) extends the upper-level moist tongue both eastward to UMN in agreement with the composite analysis, and vertically to the tropopause in contrast to the rawinsonde data, which showed drying above 8 km. The simulation places the western edge of the IOP cloud field too far to the west. The low values of RH_i found in the midtroposphere ahead of the IOP cloud field are resolved by MAPS and the model.

e. Low-level moisture features

Three other moisture layers were present at COF during the study period. The 1716, 2025, and 2330 UTC rawinsondes (Fig. 14) show the RH_i between 4 and 6 km increasing from values less than 20% to saturation after 2100 UTC. Both the MAPS analysis and the simulation resolve this moistening. The Raman lidar and CLASS rawinsondes detect a second nearly continuous moist layer between 3 and 4 km during the period. This layer is present initially in both MAPS and the simulation but vanishes after 1500 UTC.

A third layer is detected by the rawinsondes, MAPS, and model in the lowest 2 km as humid air moves northward in the southerly flow ahead of the surface trough. An accurate simulation of this southwesterly flow (Fig. 7) is important and must be validated since it brings with it stratus from the south that reaches COF after 1800 UTC (Fig. 15). The presence or lack of these clouds affects the comparison between simulated and observed radiative fields such as infrared brightness temperature. The 18-h and 21-h back trajectories terminating at 850 hPa at COF are illustrated in (Figs. 9a and 9b) where both parcels are seen to originate in south-central Texas. The initial conditions and the sim-

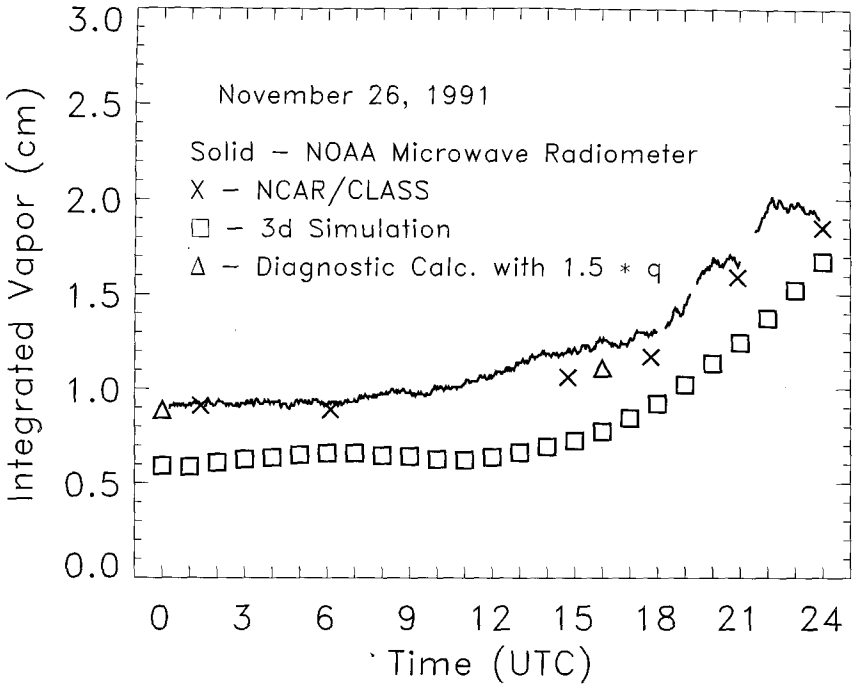

FIG. 16. Integrated column water vapor amount at COF on 26 November 1991. Solid line: derived from NOAA/ETL microwave radiometer (Shaw et al. 1995); crosses: from CLASS sondes; squares: from simulation; triangles: increased tropospheric humidity used in diagnostic calculation shown in Fig. 23.

ulation are compared with the available rawinsonde and wind profiler data at 0000, 1200, and 2100 UTC in Fig. 19. At these times, the simulated heights are within 1 dm of the observations and the simulated winds are within 2.5 m s^{-1}. The simulation shows a slight trend toward a weaker southerly component in Oklahoma at 2100 UTC. It is concluded that the winds at the level of the stratus are adequately initialized and simulated for this case study.

The RH observations for 850 hPa shown in Fig. 19a reveal high RH at Corpus Christi, Texas (CRP), and moderate RH at Del Rio, Texas (DRT), and SEP at 0000 UTC (see Fig. 2 for station locations). Low RH is found elsewhere. The tongue of moisture is advected from CRP to COF by steadily increasing 850-hPa winds during the study period. By 1200 UTC the RH is over 90% at SEP and Longview, Texas (GGG), and by 2100 UTC, 90% humidities are found as far north as COF and UMN.

The MAPS 0000 UTC analyses captures this initial pattern, though the values at DRT and SEP are 10% lower than reported. The 1200 and 2100 UTC simulations resolve the trend of increasing RH from SEP to COF as well as the sharp meridional gradients in west Texas and Arkansas. However, at 1200 UTC the 90% RH isopleth is still 200 km south of SEP and GGG and at 2100 UTC extends only into Oklahoma. It is concluded that the region of high RH probably extended farther inland at the initial time, though there are no observations for verification. This late advection of moisture to COF delays the arrival of stratus at COF and is discussed below.

Over the course of the 24-h simulation, the model developed a reasonable moisture distribution for 1200 UTC 26 November–0000 UTC 27 November in the upper troposphere via three-dimensional transport despite initializing with the dry MAPS analyses and using a dynamical model similar to MAPS. This result is perhaps due to the lack of updating the moisture distribution with NWS observations every three hours as is done in MAPS. A comparison of the MAPS 12-h simulation of moisture would be more appropriate in evaluating the modeling component of the MAPS system and initializing MM4, but the MAPS simulations are not available.

6. Cloud validation

Clouds properties were measured or inferred during FIRE-II from active and passive sensors aboard satellite and aircraft, and at the surface. The characteristics and capabilities of these instruments have been described in the papers in the special FIRE IFO II issue of the *Journal of the Atmospheric Sciences* (1 December 1995). As was the case for water vapor, none of the platforms or sensors individually

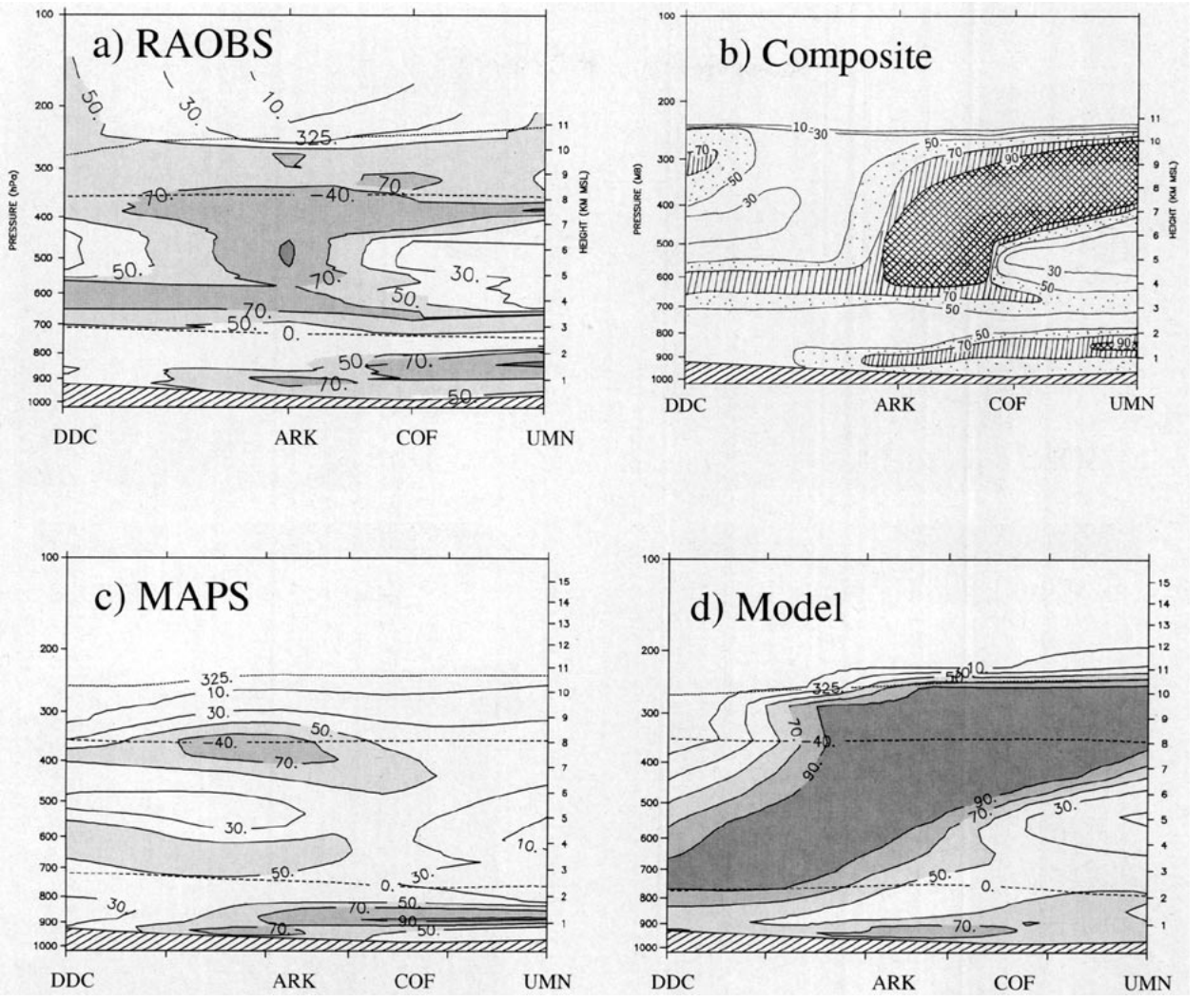

FIG. 17. As in Fig. 11 except at 2100 UTC and across the tongue of moisture over Kansas and Oklahoma (thick solid line in Fig. 13). (a) Analysis of corrected NWS rawinsonde data from Dodge City, Kansas (DDC), and Monett, Missouri (UMN), and NCAR CLASS data from ARK and COF; (b) as in (a) but modified to account for UTH_{GOES} and radar data; (c) MAPS analyses; and (d) simulation.

yields the regional-scale three-dimensional distribution and amount of cloud necessary for a quantitative verification of the cloud simulation. The various measurement techniques either lack one or two dimensions, are not calibrated, or must infer the cloud amount from a radiative measurement. The aircraft make nearly direct measurements of liquid and ice water content and have high resolution in the vertical and temporal dimensions but only remain aloft for hours at a time. The surface passive instruments have high temporal resolution, low vertical resolution, and measure clouds indirectly via their effect on radiation. The surface active instrumentation have high vertical resolution plus the ability to scan. Only the satellite sensors yield the regional view of the distribution of clouds that is crucial for validation of the simulations. However, these lack a capability for vertical profiling of the cloud field. Thus, validation of the cloud simulation is done on an ad hoc basis as the data permit. In this section the observed (or inferred) and simulated physical properties of the clouds are compared. These include cloud boundaries sensed by lidar and radar, aircraft observations of IWC, IWC inferred from radar, and cloud-top height inferred from GOES. The simulated and observed radiative fields are compared in the next section.

Figure 20 shows the simulation of the IOP cloud field as it progresses eastward across Kansas and the stratus moving northward across Texas. The north–south axis of the cloud field crosses COF at 2100 UTC. At 2100 UTC, the highest water contents are found to the north in Nebraska and to the south in Texas. The horizontal distribution is in qualitative agreement with the GOES

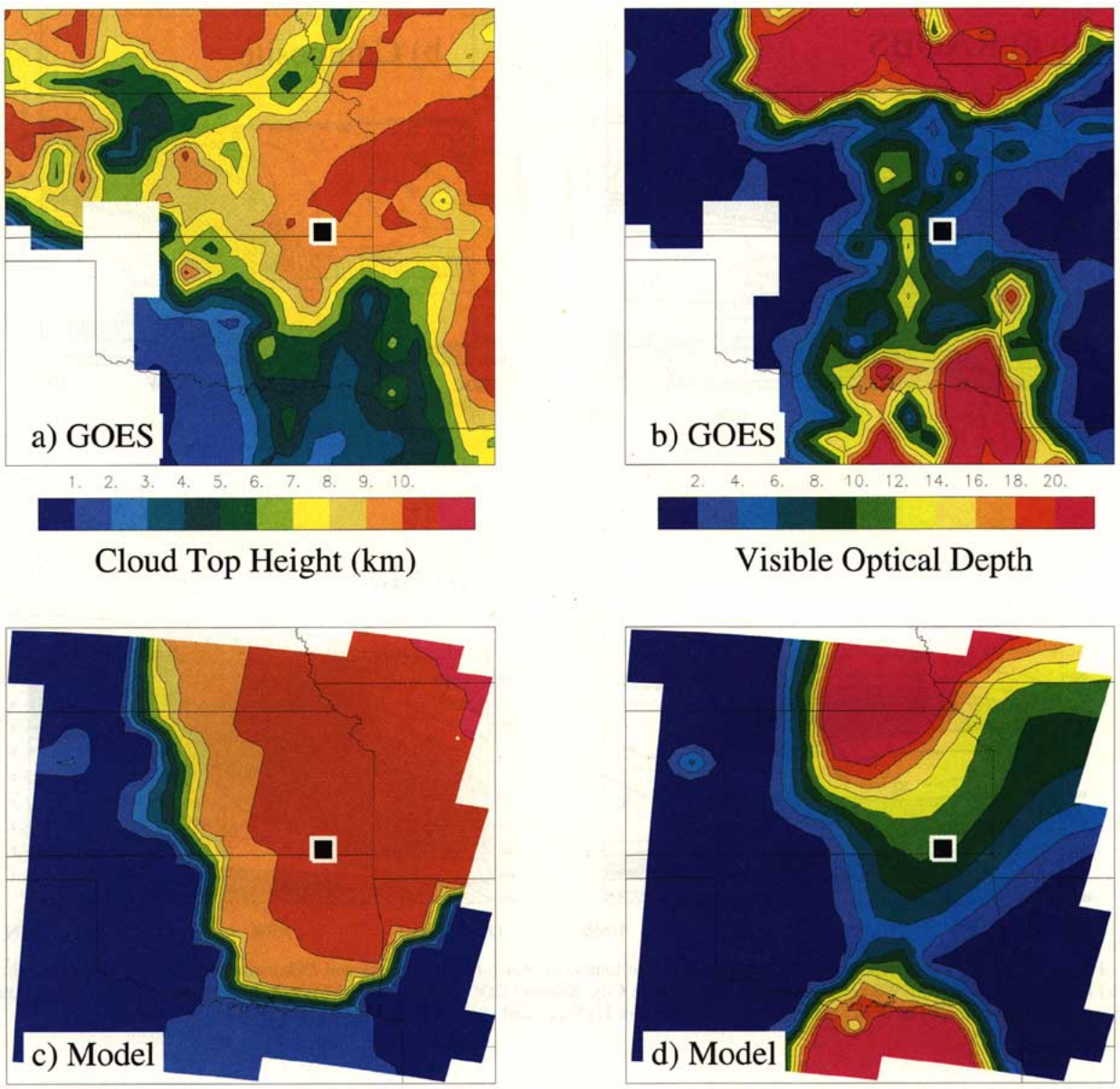

FIG. 18. Cloud properties at 2100 UTC derived from GOES (top row) and simulated (bottom row). Left column: cloud-top height (km ASL), contoured every 1 km from 0 to 12 km. Right column: visible optical depth, contoured every 2 from 0 to 22.

data (Figs. 1c and 13a). The model also simulates the generally cloud-free conditions from western Nebraska to western Texas.

A meridional cross section through COF at 2100 UTC (Fig. 21) reveals the two separate cloud layers and shows that the simulated stratus has not yet reached COF. Peak cloud concentrations of 73 mg m^{-3} are found in the cirrus just north of COF, while concentrations 500 mg m^{-3} are found in the stratus at the Oklahoma–Texas border.

Matrosov et al. (1995) employed a diagnostic relationship between radar reflectivity and ice water content to infer the mixing ratios contoured in Fig. 22a. Before the cloud deepens at 1900 UTC, values range between 3 and 30 mg m^{-3} with the lowest values at cloud top. Afterward, values as high as 100 mg m^{-3} are common and a few as large as 300 mg m^{-3} are inferred. These data have 37-m vertical resolution and 30-s temporal resolution and detect the details of the cloud structure.

Kinne et al. (1996) inferred the individual values of IWC shown in Fig. 22b from the NCAR King Air and Sabreliner particle probe data averaged over periods of 1–34 min (6–60 km) during vertical profiles and con-

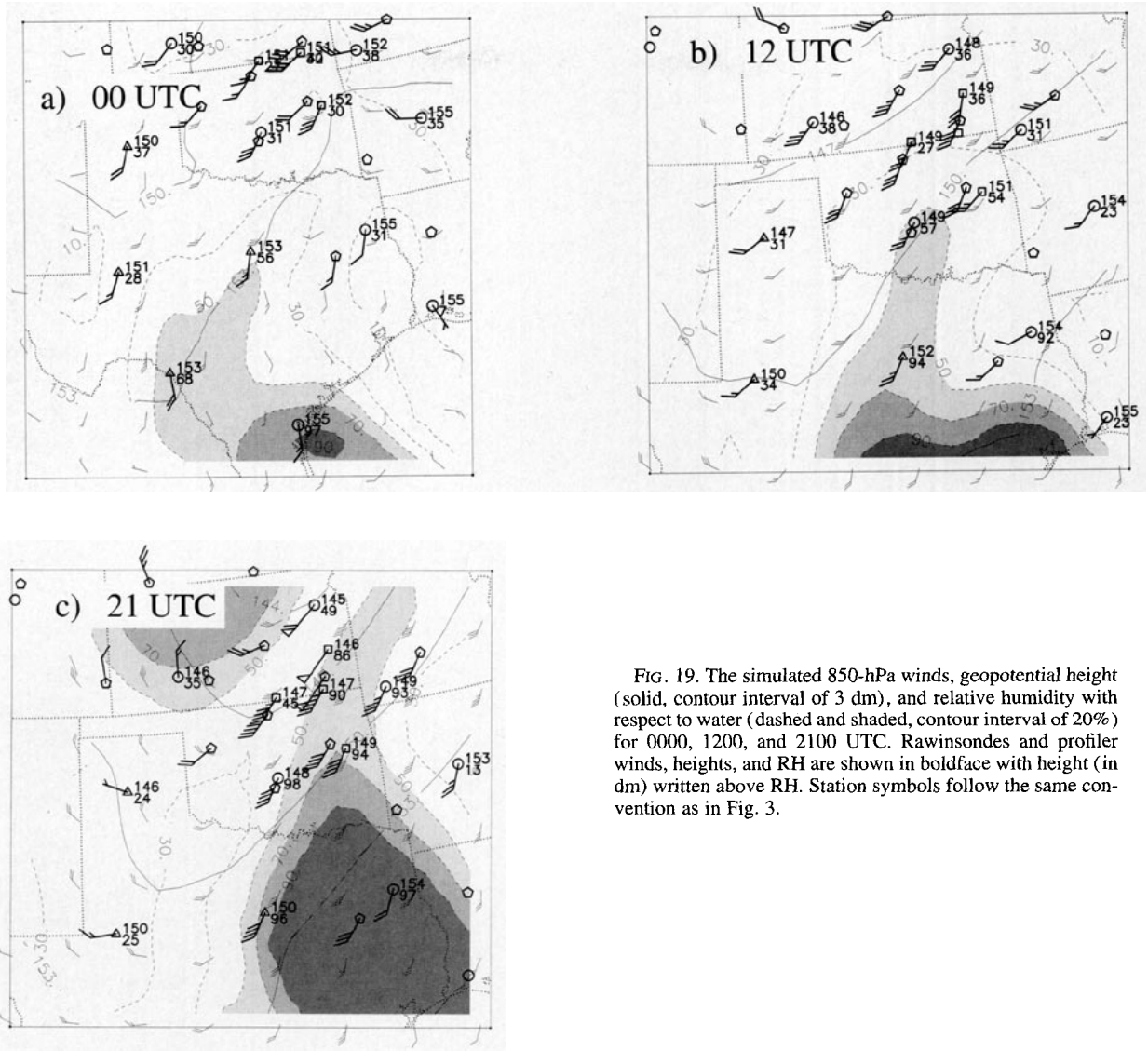

FIG. 19. The simulated 850-hPa winds, geopotential height (solid, contour interval of 3 dm), and relative humidity with respect to water (dashed and shaded, contour interval of 20%) for 0000, 1200, and 2100 UTC. Rawinsondes and profiler winds, heights, and RH are shown in boldface with height (in dm) written above RH. Station symbols follow the same convention as in Fig. 3.

stant-altitude legs over COF. Kinne et al. also inferred IWC from ice replicator sonde data (Heymsfield and Miloshevich 1995). The aircraft and ice sonde values range from 0 to 35 mg m^{-3}, with the lowest values at cloud top, and are generally of the same order of magnitude as those inferred by Matrosov et al. (1995), though at times the latter show values higher than 100 mg m^{-3}. The aircraft and sonde data represent temporal and spatial averages and are incapable of detecting the highest values inferred by Matrosov et al.

The time section of simulated cloud concentration at COF from 1600 UTC 26 November to 0000 UTC 27 November are compared in Fig. 22b with the NOAA cloud boundaries, inferred IWC values, and the aircraft IWC values. No clouds were simulated at COF previous to 1600 UTC. The lack of simulated clouds at 0900 UTC is due to the absence of the moist feature north of LBF in the initial conditions (Fig. 10). The simulation duplicates several of the features observed by lidar and radar (Fig. 15) including the onset around 1600 UTC, the cloud-top height during the first four hours, the lowering of the cloud base during the period, and the stratus layer between 1 and 2 km. The simulated values of cirrus IWC are similar to the observations before 2000 UTC or at altitudes below 7 km. The peak simulated concentration of 73 mg m^{-3} occurs at 2200 UTC at 7.2 km. After 2000 UTC and above 8 km, the simulated values are several times larger than the aircraft data. In particular, the simulated IWC is as high as 30 mg m^{-3} up to the tropopause at 10.5 km, whereas the aircraft and remote sensing data suggest values less than 10 mg m^{-3} above 9 km. The simulated cloud base is up to 1 km too low, except after 2200 UTC. The radiative impact of the overprediction of IWC and of

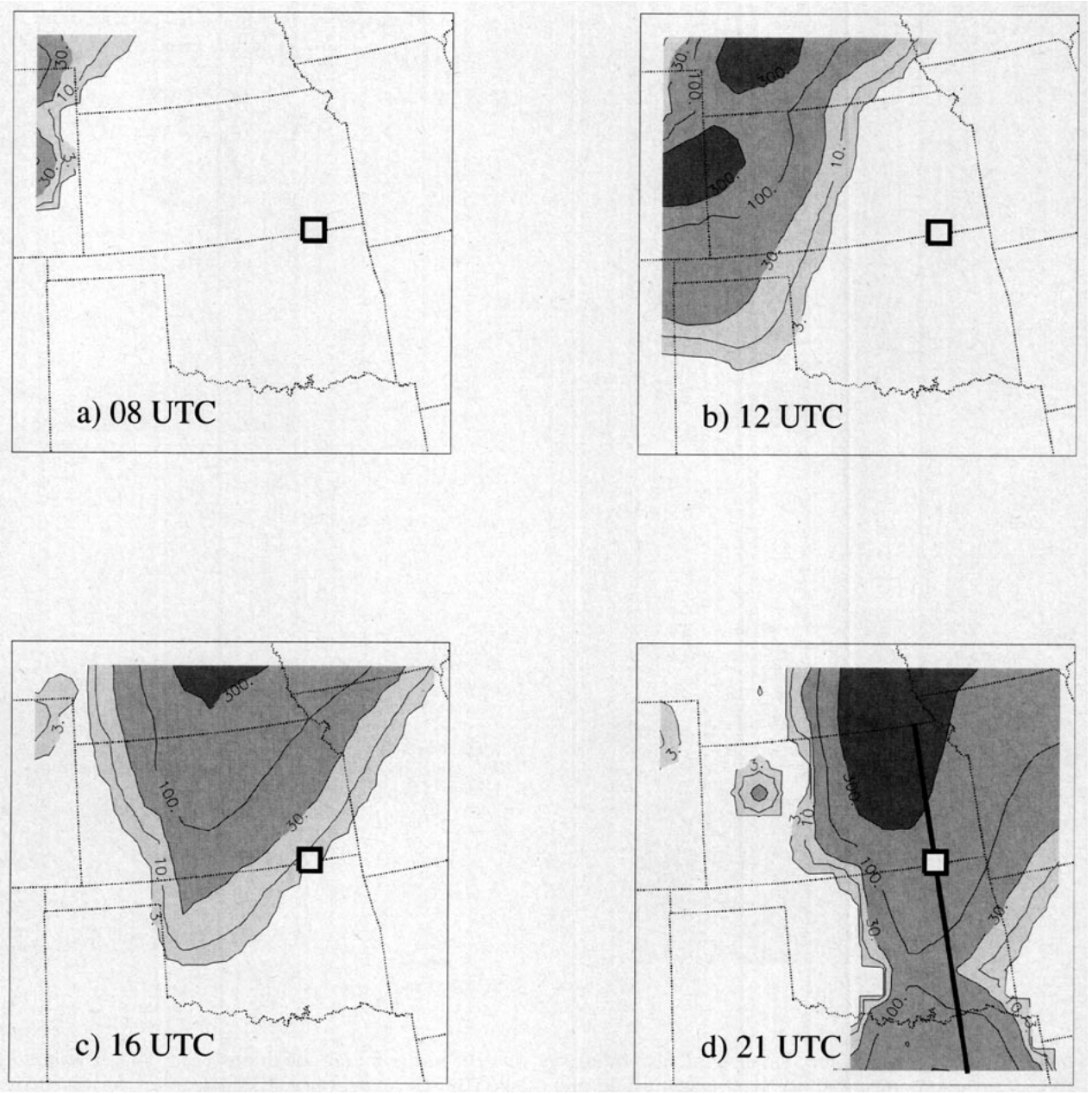

FIG. 20. Vertical integral of the simulated condensed water at (a) 0800 UTC, (b) 1200 UTC, (c) 1600 UTC, and (d) 2100 UTC. Contour intervals of 3, 10, 30, 100, 300, and 1000 g m^{-2}. The thick solid line in (d) shows the location of the cross section in Fig. 21.

errors in cloud top and base are discussed in next section. The model does not simulate the intermittent midtropospheric clouds at 1400–1600 UTC or the lowering of the cloud top at 2300 UTC. The stratus clouds are late in arriving at COF.

In Figs. 18a and 18c, the cloud-top height at 2100 UTC derived by Minnis et al. (1993) is compared with the simulated cloud-top height, defined as the height of the top of the first layer with a visible optical depth of greater than 0.1. The analysis of Minnis et al. shows an irregular pattern of cloud-top heights of 9–11 km over all but the southwest corner of the analysis domain. The simulation shows a more uniform pattern with higher cloud tops ranging from 10 to 11 km. Clouds are not simulated in the northwest corner of Fig. 18c since the initial high humidity and cloudiness in the intermountain west is underestimated (e.g., Figs. 1 and 13). Both the GOES data and the model show stratus cloud tops over Texas and Oklahoma between 1 and 2 km.

The only regional analysis that quantifies the cloud liquid water or ice amount is the GOES analyses of

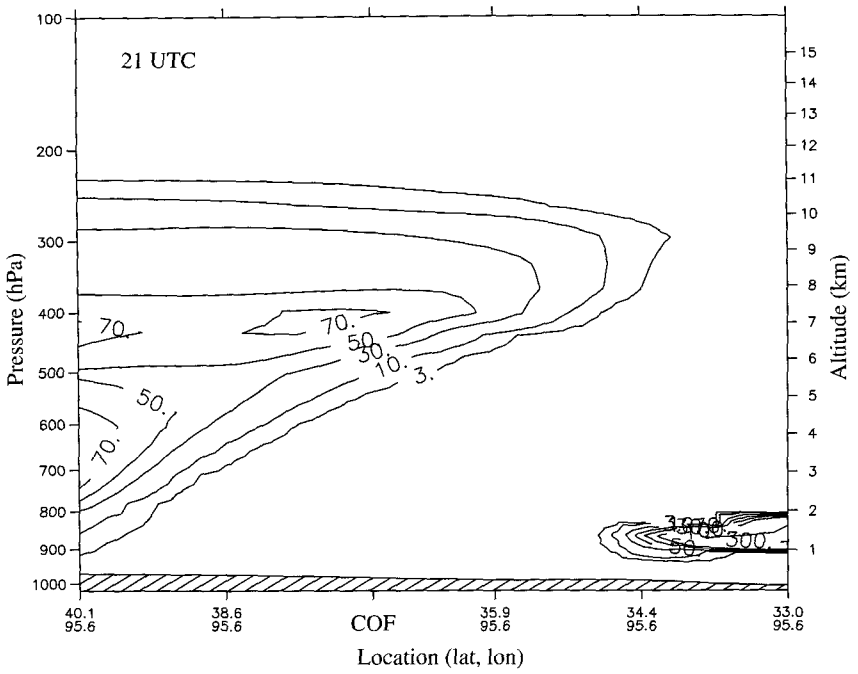

FIG. 21. Cross section of modeled concentration of ice plus cloud water from 40° to 30°N along 95.6°W (the thick line shown in Fig. 20) at 2100 UTC. Contour intervals of 3, 10, 30, 50, 70, 100, 300, and 500 mg m^{-3}.

visible optical depth by Minnis et al. shown in Fig. 18b. At 2100 UTC, τ_{vis} is 2–14 in the IOP cloud field over eastern Kansas with a value of 5 at COF. The size-resolving radiation model calculation [discussed in section 2d(5)] yielded τ_{vis} of 4.9 at COF at this time. Estimates from surface instrumentation ranged from 2 to 5 (Shiobara et al. 1996). The model predicts τ_{vis} between 8 and 12 for the same area (Fig. 18d). Thus, the comparison to satellite data reveals that while the simulation is in qualitative agreement with the observations, the simulated cloud is too high and thick, not just at COF, but over a larger region.

7. Radiative transfer validation

Often only the radiative properties at the top of the atmosphere are evaluated in models. However, additional aspects of atmospheric radiative transfer are relevant to this simulation. These include the atmospheric heating rates and surface fluxes that are important since these influence the dynamics and clouds. In this section, the radiative aspects of the simulation are discussed and validated, first at COF and then on a regional scale, as the data permit.

a. Simulation at COF

Figure 23 shows the infrared (~10–11 μm) brightness temperatures T_{BS} at the surface at COF measured by the NASA/ARC narrow field-of-view radiometer (NFOV) (Pilewskie and Valero 1993) and the NOAA/ETL single-band filter radiometer (PRT5) (Shaw et al. 1995). A warm bias in the PRT5 data at temperatures below 205 K has been corrected as described in Shaw et al., but the PRT5 T_{BS} are still 5 K warmer than the NFOV T_{BS} prior to 1800 UTC. The reason for the discrepancy is unclear but may be due to different bandwidths or calibration temperatures. The bandwidths for the PRT5 and NFOV are 1.5 and 0.9 μm, respectively. The PRT5 is calibrated at about 205 K, while the NFOV is calibrated at a nearly continuous range of temperatures between 193 and 293 K. After 1900 UTC, T_{BS} is warmer than 215 K and the two radiometers agree. The cold temperatures detected by the PRT5 early in the day are typical for a dry atmosphere. Recall that the precipitable water amounts were less than 1 cm during this period (Fig. 16). The observations show a trend toward moister conditions from 0000 to 1600 UTC with brief periods of cirrus at 0300 UTC and again at 0900–1000 UTC. Accordingly, T_{BS} slowly increases during this time and shows temporary 5 K increases when the cirrus are present. After 1600 UTC, the IOP cirrus reaches COF and then deepens and T_{BS} increases to 245 K. At 2000 and 2200–2300 UTC, stratus are present and T_{BS} exceeds 275 K. The T_{BS} from the size-resolving radiation model calculation [section 2d(5)] is 248 K for 1941–2046 UTC and similar to the observed values during that period, except when stratus were present.

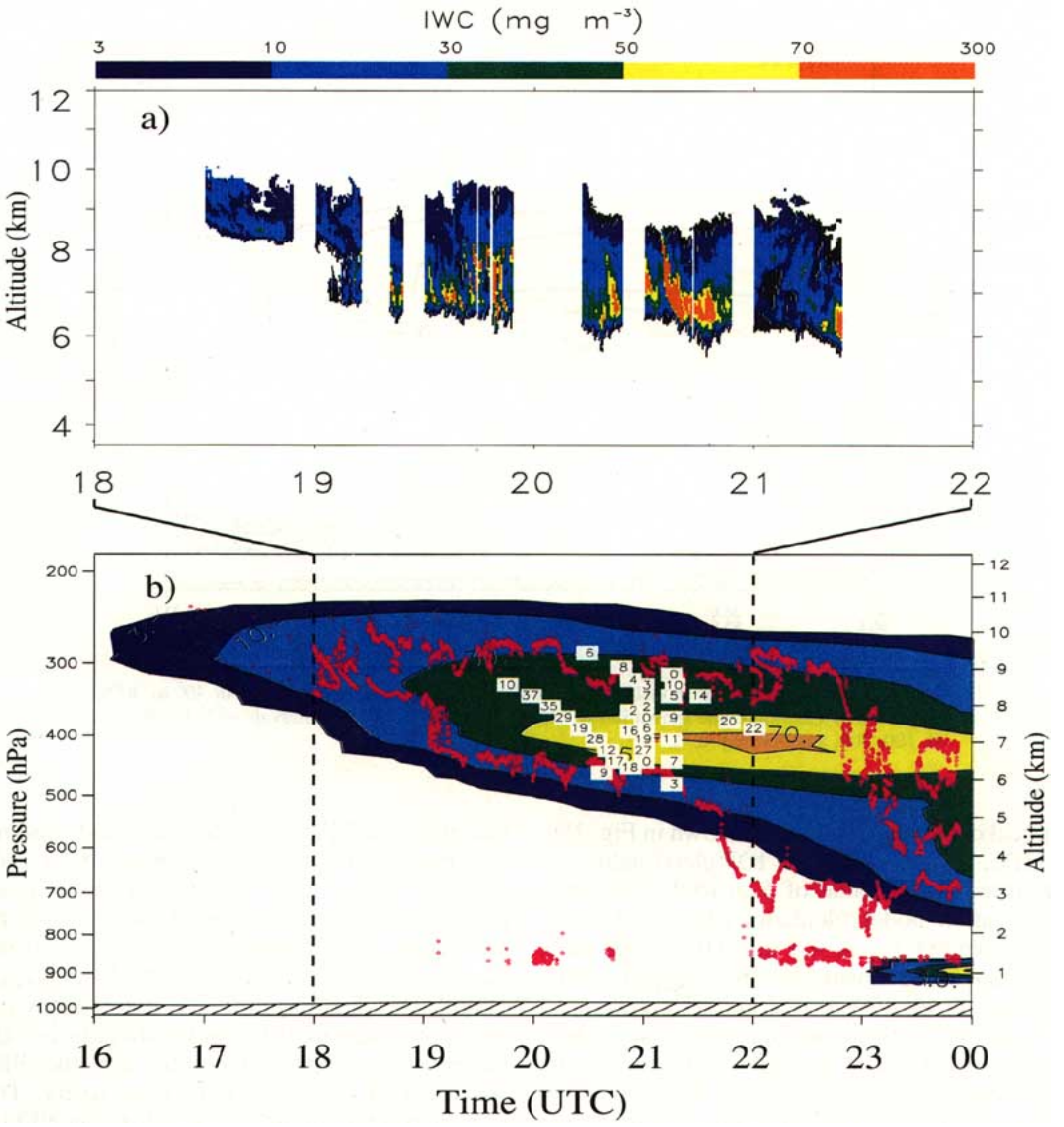

FIG. 22. Time section of concentration of ice plus cloud water (in mg m^{-3}) at COF from 1200 UTC 26 November to 0000 UTC 27 November: (a) concentrations inferred from radar reflectivity by Matrosov et al. (1995); (b) simulated concentrations combined with lidar and radar cloud boundaries (dots; from Fig. 15) and concentrations (in white boxes) from NCAR aircraft data (6- to 60-km averages); contour intervals of 3, 10, 30, 100, 300, and 500 mg m^{-3}.

The simulated T_{BS} are plotted at hourly intervals in Fig. 23. During the first 16 h of the simulation when clear skies prevail, T_{BS} is 12 degrees colder than the PRT5 values. This result was expected since the simulated precipitable water at COF is only 60% to 70% of the observed values (Fig. 16). Accordingly, the simulated atmospheric emission is less and T_{BS} is colder than observed. Given the correct precipitable water, the model does simulate the observed T_{BS}. This is demonstrated with diagnostic calculations for COF at 0000 and 1600 UTC in which the simulated humidity at all levels of the troposphere is increased by 50% so that the precipitable water matches the observed amounts (Fig. 16). The resulting T_{BS} for these two times are shown in Fig. 23 and are now identical to the observed T_{BS}. Since there is little energy in this region of the spectrum at cold cirrus temperatures, a 10 K difference in the 10–11-μm brightness temperature equates to only a 1.7 W m^{-2} difference in the downward flux at the surface. Even over the entire window, a 10 K difference equates to only 3 W m^{-2}. For the entire infrared spectrum, the difference is 12 W m^{-2}.

By 1700 UTC the IOP cloud field reaches COF and, for the next several hours, the simulated T_{BS} is higher than observed since the cloud base is lower (Fig. 22).

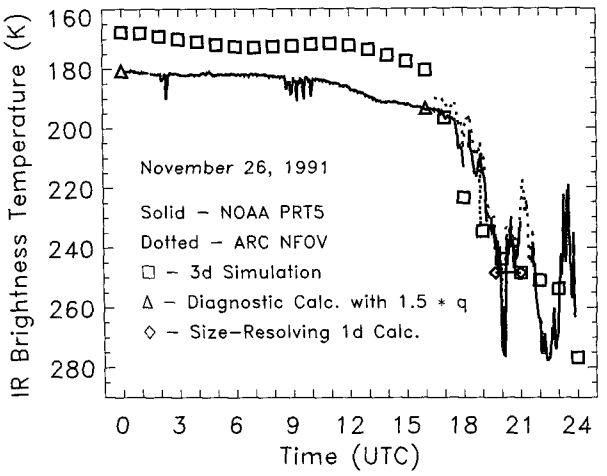

FIG. 23. Infrared (~10–11 μm) brightness temperature at COF on 26 November 1991. Solid line: corrected NOAA/ETL PRT5 infrared radiometer data (Shaw et al. 1995); dashed line: NASA/ARC NFOV infrared radiometer (Pilewskie and Valero 1993); squares: 3D model simulation; triangles: diagnostic 1D model simulation with increased tropospheric humidity; and diamonds: value from calculation with size-resolving radiation model using observed cloud size distributions and CLASS COF sounding [section 2d(5)].

After 1900 UTC, the simulated T_{BS} is within 10 K of both the observations and the size-resolving calculation, except when stratus are present. Differences of 10 K in the simulated and observed T_{BS} at these warm temperatures equate to 5.3 W m^{-2} downward flux in the 10–11-μm band at the surface. This tripling of the flux error at warm temperatures is significant but does not apply to all infrared wavelengths since gaseous absorption and emission in the near-surface layers still dominate the surface flux at most infrared wavelengths. For the entire infrared spectrum, the difference is 13 W m^{-2}. The model does not simulate the stratus at COF until 0000 UTC 27 November, so the simulated T_{BS} remains colder than 260 K until that time and errors are as large as 25 K. The stratus are sufficiently low that the entire infrared spectrum is affected. The downward infrared flux at the surface is increased 38 W m^{-2} by their presence.

The time series of combined solar and infrared heating rates at COF (Fig. 24) show a broad range of radiative heating profiles as the clouds at COF change from optically thin to optically thick. From 1600 to 1800 UTC, the cloud is relatively thin and midcloud infrared heating exceeds cloud-top infrared cooling. Solar heating rates exceed 3 K day^{-1} from 1700 to 2200 UTC and the peak solar heating rate of 9 K day^{-1} occurs two hours after local noon since the cloud optical depth is continually increasing. At 1800 UTC, the solar and infrared heating combine for a total heating rate of 17 K day^{-1} at 9 km. After 2000 UTC the cloud becomes sufficiently thick that infrared cloud-top cooling dominates the heating profile. The peak total cooling of −16 K day^{-1} occurs at 2300 UTC when the cloud is thickest and the solar heating is small.

The aircraft data allow indirect verification of the radiation simulation at COF from 2000–2100 UTC. In section 2d(5) the observed size distributions and atmospheric profiles were used in a size-resolving radiation code to calculate heating rates and surface fluxes and the results were presented earlier in Fig. 5 and Table 1. These same profiles are shown in Fig. 25 along with the simulated profiles for 2000 and 2100 UTC. The simulated profiles of IWC have a peak value similar in magnitude and location to that of the observations, but the simulated cloud top is 1 km higher than observed. The diagnosed r_e decreases with altitude as in the observations. The simulated β_e profile has reasonable peak values, but these occur 1.4 km higher than observed. As a result, the magnitudes of the maximum solar heating and infrared cooling rates are reasonable, though displaced 1.5 km higher than observed. At cloud base, the model overestimates both IWC and r_e. However, β_e involves the ratio IWC/r_e [e.g., Eq. (1)] so the magnitudes of the simulated profiles of β_e and heating rates match the observations.

b. Regional simulation

Evaluation of the simulated radiative fields over the IOP area is done by comparison with the GOES analyses of Minnis et al. (1993). The GOES analysis of 11-μm brightness temperatures at the top of the atmosphere T_{BT} at 2100 UTC (Fig. 26a) reveals T_{BT} of 240 to 250 K over southeastern Kansas. These temperatures are found in the atmosphere at altitudes of 6.5–8 km or well below the observed cloud tops of 9–11 km (Figs. 15 and 18a), indicating an optically thin upper cloud. The size-resolving radiation model calculation [section 2d(5)] yielded T_{BT} of 233 K at COF. In contrast, the model predicts T_{BT} of less than 225 K (Fig. 26c), indicating once again that the simulated cloud is too high and thick over the entire region.

The simulated visible albedo is compared with the GOES analysis in Figs. 26b and 26d. The analysis shows detailed structure and values of 0.4–0.75 in the IOP cloud field of eastern Kansas with 0.5 at COF. Highest values are found in Nebraska, southeast Oklahoma, and northeast Texas. The simulated horizontal distribution is in qualitative agreement and shows the trend of lower albedo of the IOP cloud field over Kansas and the high albedo of both the Nebraska cloud field and the stratus in Texas and Oklahoma. At COF the albedos are greater than 0.7, again due to the high simulated optical thickness. The GOES albedos in the west of less than 0.2 are not simulated since the specified surface albedo there is never less than 0.23. The observed, calculated, and simulated albedos for COF at 2000–2100 UTC were listed in Table 1. There is agreement between the size-resolving calculation and the GOES analysis, but the simulated values are higher due to the higher IWC amounts.

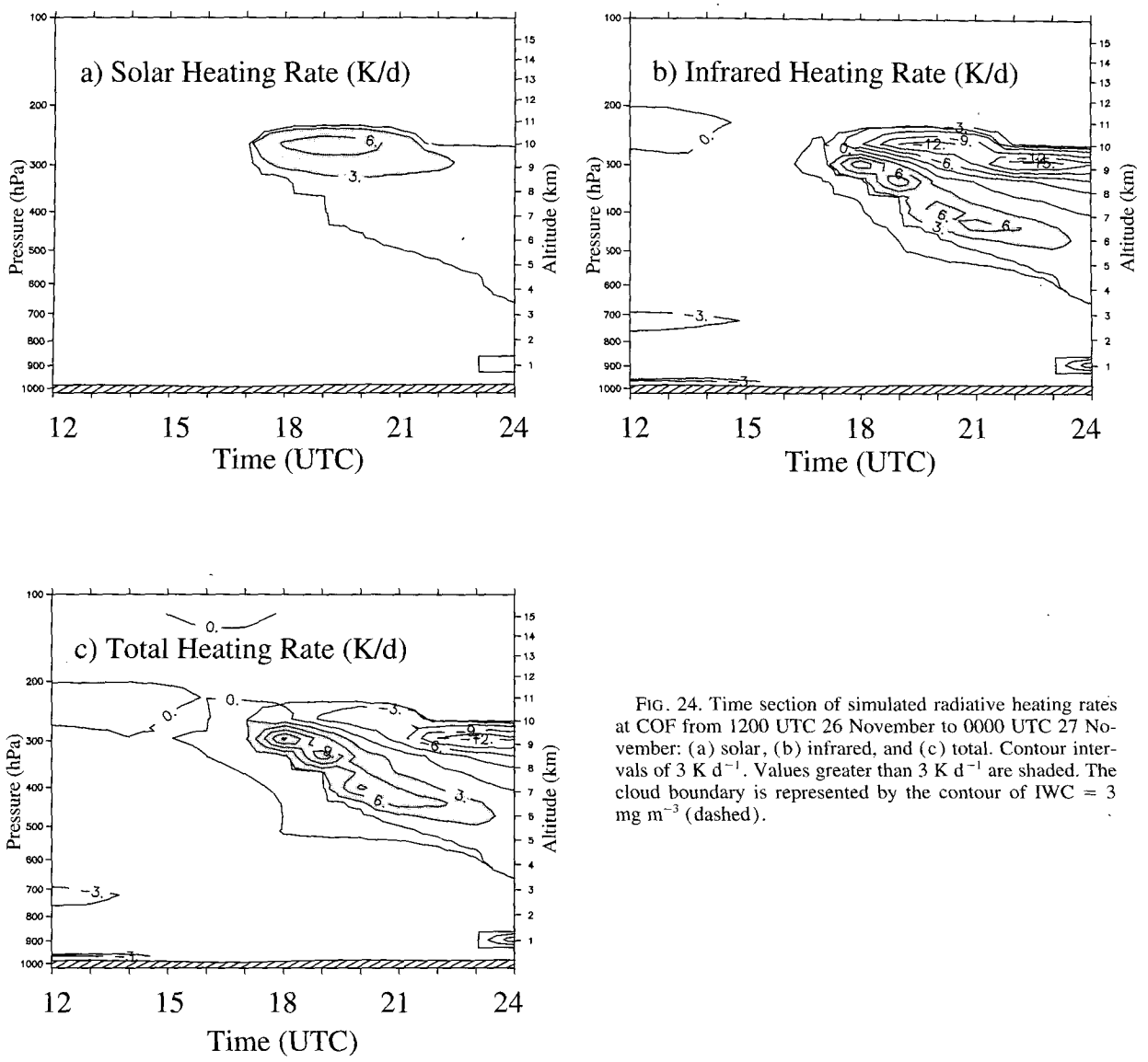

FIG. 24. Time section of simulated radiative heating rates at COF from 1200 UTC 26 November to 0000 UTC 27 November: (a) solar, (b) infrared, and (c) total. Contour intervals of 3 K d^{-1}. Values greater than 3 K d^{-1} are shaded. The cloud boundary is represented by the contour of IWC = 3 mg m^{-3} (dashed).

8. Summary and conclusions

Observations from a wide variety of instruments and platforms are used to validate many different aspects of a cirrus cloud simulation. The simulation is made with mesoscale dynamical model utilizing a simplified bulk water cloud scheme and a spectral model of radiative transfer. Expressions for bulk cirrus optical properties for solar spectral intervals as functions of wavelength, ice water content, and effective particle radius, are modified or derived to match those of the midlatitude cirrus observed during FIRE-I and FIRE-II. The expressions are also modified for use in infrared spectral intervals. These approximations compare favorably with explicit size-resolving calculations of the optical properties of observed cirrus size distributions. Based on FIRE-I and FIRE-II data, an expression for effective particle radius as a function of both temperature and ice water content is developed and provides a better fit than expressions involving temperature or ice water content alone. One-dimensional radiative transfer calculations with these approximations compare well with explicit size-resolving calculations. For this case study (and perhaps for most other mesoscale applications), the differences between the observed and simulated radiative quantities are due more to errors in the prediction of ice water content than to the errors in the optical properties or the radiative transfer solution technique.

During the 26 November 1991, Intensive Observing Period of FIRE-II, the shortwave trough situated over the northern plains moved southeastward so that it coincided with the axis of the large-scale trough

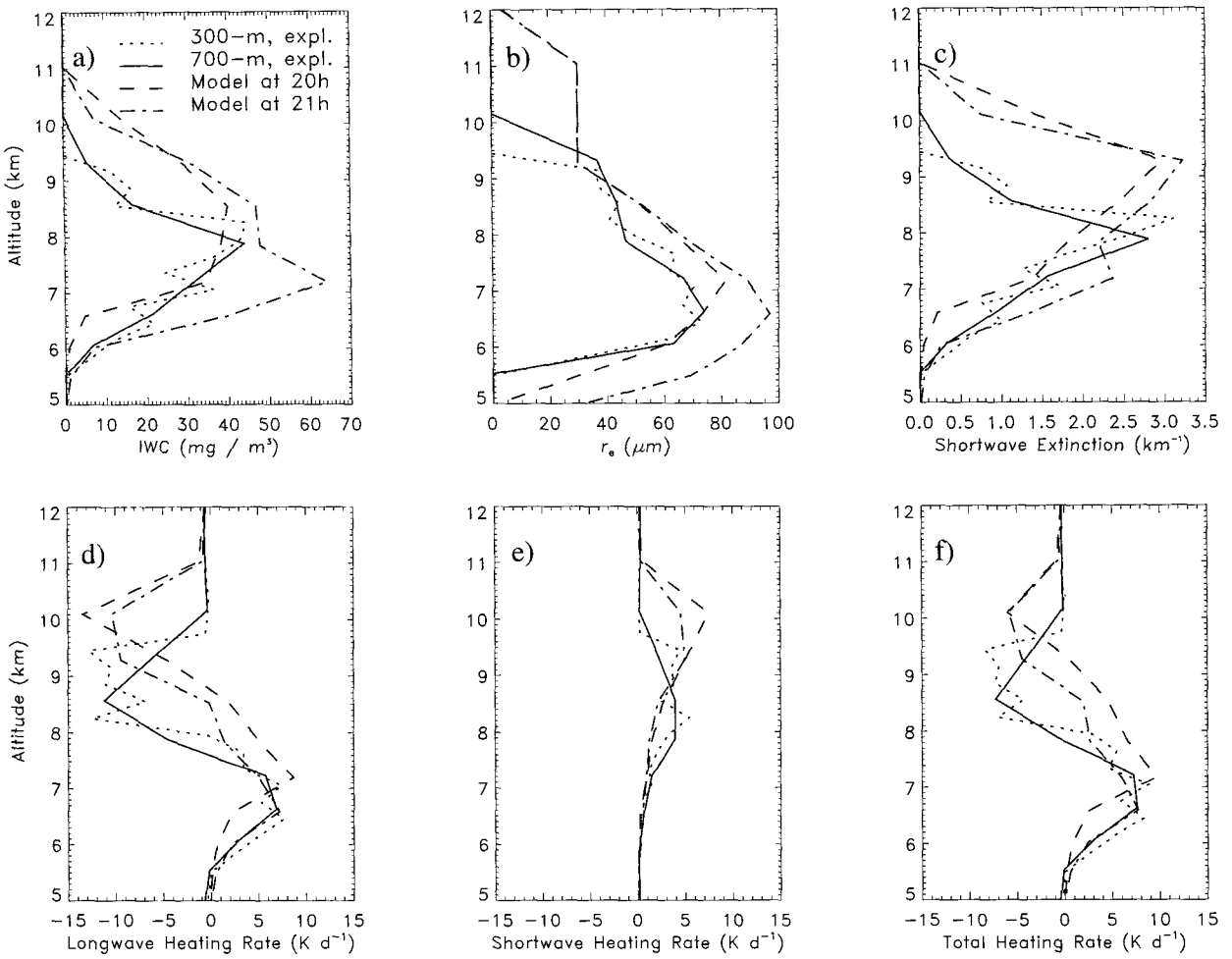

FIG. 25. As in Fig. 5 with the dotted and solid lines again representing observations or explicit calculations with the size-resolving radiation model. Here, the dashed and dot–dash lines are the simulated profiles for COF at 2000 and 2100 UTC, respectively.

situated directly over COF. The eastward movement of this shortwave and a jet streak entering Kansas resulted in moderate upward motions and cloud formation in the IOP region, beginning around 1700 UTC. During the latter hours of the IOP, stratus was also present at COF and is of interest because of its strong radiative effects.

The model accurately simulates the dynamics in the IOP region, except that the jet and trough passage are one hour late and the midtropospheric vertical velocities, which cause the cloud formation, persist one to two hours too long. These forecast errors lead to errors in the simulated cloud properties that outweigh or obscure those caused by the cloud parameterization. Additionally, the lack of the strong subgrid-scale vertical motions in the model reduces the likelihood of formation of large precipitating particles. Hence, removal of ice from the cloud is retarded when coarse model resolution is used. This mechanism is accounted for in the bulk water cloud scheme by the conversion of ice to snow, which then precipitates. It is possible, however, that the existing conversion and sedimentation rates are not applicable to midlatitude winter cirrus. The suitability of these processes can be studied using the microphysical data available from FIRE and other field programs.

Trajectory analyses reveal Pacific origins for 24-h back trajectories in the upper troposphere, indicating that a large area must be sampled in order to adequately initialize a model of wintertime midlatitude cirrus. Rawinsonde, Raman lidar, and satellite data are combined to produce a time section of humidity at COF during the IOP. The Raman and GOES data show that the upper troposphere at COF and other locations covered by the IOP cloud field was more moist than indicated by the rawinsonde data. In other instances, the rawinsonde humidities are too high. The rawinsonde humidity data are not robust, and corroborating data must be utilized before rawinsonde data can be accepted. Though incomplete when used alone, the Raman and

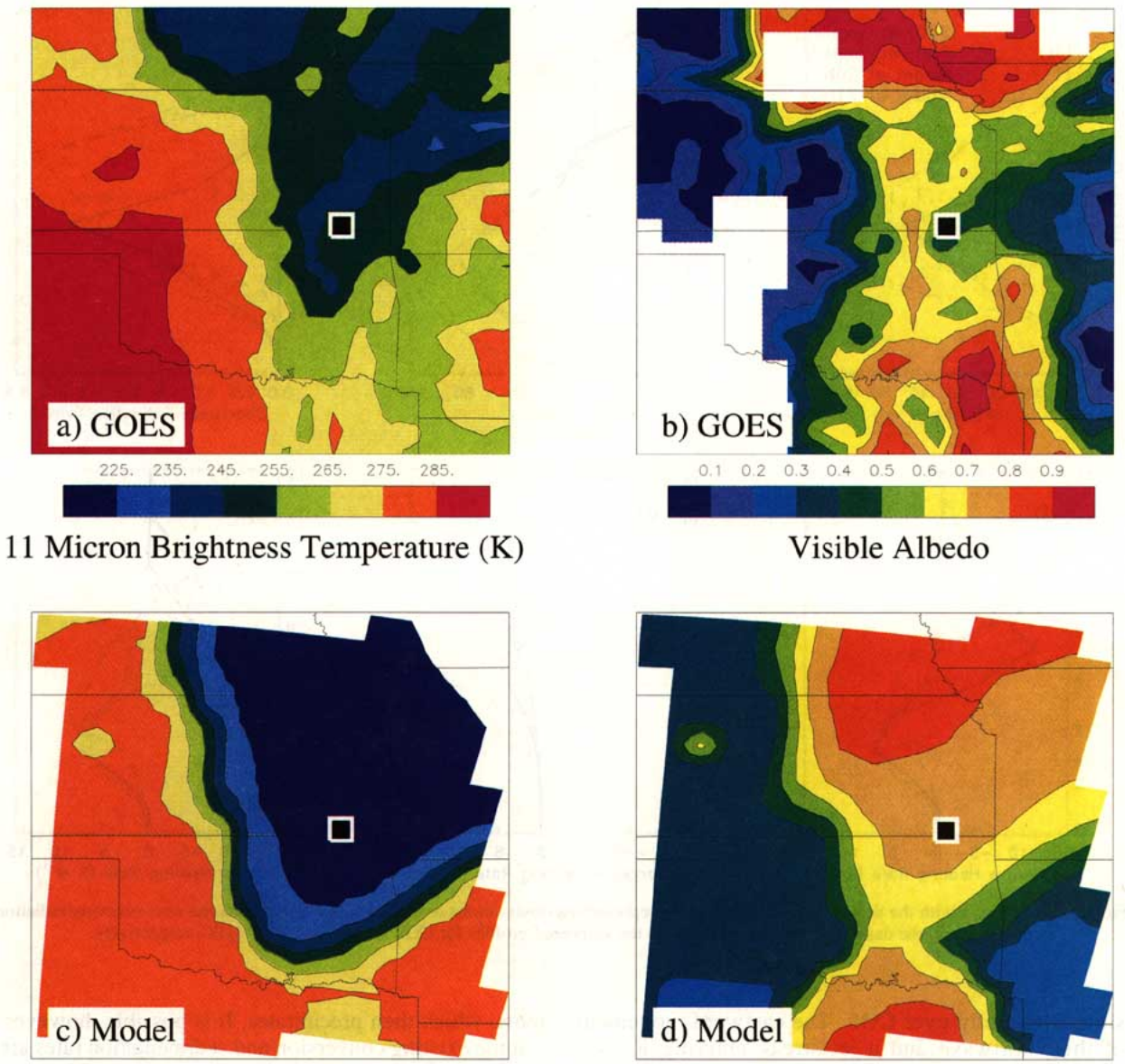

FIG. 26. Cloud properties at 2100 UTC derived from GOES (top row) and simulated (bottom row). Left column: 11-μm brightness temperature (K), contoured every 10 K from 215 to 295 K. Right column: visible albedo, contoured every 0.1 from 0.0 to 1.0.

GOES data are invaluable for their resolution and coverage.

Since rawinsonde humidities at temperatures below −40°C (~8 km) were not being transmitted over AFOS at the time of the experiment, no humidity data were available for input into the MAPS data assimilation cycle at those temperatures. Unfortunately, the 1991 version of MAPS inserted bogus rawinsonde values of 5% relative humidity when upper-level values were missing, resulting in a significant dry bias in the analyzed upper-level relative humidity. This procedure has since been eliminated in MAPS, along with many other improvements in the version of MAPS now running operationally at NCEP as the Rapid Update Cycle (Benjamin et al. 1994, 1995). However, as a result of this problem in the 1991 version, the MAPS humidities were generally less than 50% of the GOES values at temperatures below −40°C but reasonable at warmer temperatures. The simulation was initialized with this dry distribution, yet over the course of 24 h, produced a distribution that more closely resembled the GOES water vapor data than did the corresponding MAPS *analysis.* It is likely that the MAPS *simulations* also produced better water vapor distributions, but these were not available for comparison. While it is true that the NWS now transmits the cold-temperature humidity

data, the data are so poor (D. Westphal 1996, manuscript submitted to *J. Atmos. Oceanic Technol.*) that assimilation of these data may degrade analyses.

Considering the spacing of rawinsondes and the frequency of their release, important small-scale moisture features will continue to go undetected. The cloud field observed at COF at 0900–1000 UTC and originating north of LBF at 0000 UTC was undetected by rawinsonde and absent in the conventional analyses. An initial analysis containing features such as these is essential for detailed comparisons of regional-scale simulations with data from today's high-resolution satellite and remote sensors. Even the main IOP moisture feature went unresolved despite the 3-h radiosonde release schedule and four supplemental release sites during the IOP.

Note that this problem will persist even if accurate radiosonde humidity sensors are developed. Barring an unlikely increase in radiosonde density and accuracy, satellites provide the only hope for accurate, high-resolution, model initialization. The assimilation of retrievals of precipitable water from the Television and Infrared Observational Satellite (TIROS) Operational Vertical Sounder (TOVS) or specific humidity profiles should improve the vapor initialization over oceans. However, variational techniques may better directly utilize the satellite radiances that peak in the upper troposphere (McNally and Vesperini 1995). These more accurate fields could then propagate inland, provided that the analysis over land is not degraded by subsequent assimilation cycles. Further improvement may come by the use of vapor-tracked winds (Nieman et al. 1996) to improve the upper-tropospheric steering flow, thereby indirectly improving the moisture distribution. For the present, data analysis systems should rely more heavily on the upper-tropospheric water vapor distribution of the previous forecast than on the rawinsonde observations, keeping in mind that some models may have a strong moistening or drying bias.

Despite the defects in the initial moisture distribution and in the simulated dynamics, the simulated distribution and concentration of ice in the IOP cloud field compares favorably with radar, lidar, and aircraft data and with GOES-retrieved cloud properties. If the defects had not been revealed, this success could lead to unjustified efforts to modify or tune the model's microphysics so that the simulation more closely matches the observations.

There are some important differences between the simulated cloud and the observations. For example, the simulated IWC at cloud top and the height of the cloud top were higher than observed, an unexpected result considering the dry initial conditions in the upper troposphere. Vertical advection by the simulated persistent midtropospheric vertical velocities offsets the initially dry upper and midtroposphere.

The use of a spectral radiative transfer model allows comparison with broadband and spectral sensors. In this paper, comparisons are made between simulated quantities and those detected or inferred by GOES and microwave and infrared radiometers. The GOES-derived variables are cloud albedo, optical depth, and top-of-the-atmosphere 11-μm brightness temperature, and the 6.7-μm brightness temperature. The cloud optical depth analysis is the only regional quantitative measure of cloud liquid water or ice amount. In comparison, the simulated optical depth at COF is high, but the reason for this is not immediately obvious since both the analysis and the simulation invoke a variety of microphysical and optical assumptions [e.g., Eq. (7)]. Hence, measurements of other moments of the cloud distribution are required. These include the aircraft measurements of IWC, calculated extinction, and radar- and lidar-inferred IWC. From these it is found that the differences in optical depth and visible albedo are due to high IWC at cloud top. Comparison with the GOES cloud-top heights and 11-μm brightness temperatures also shows that the simulated cloud tops are too high.

The infrared and microwave brightness temperatures at the surface provide an alternative measure of the water vapor profile, cloud base, and radiative calculations. Clear-sky errors of 12 K in T_{BS} are shown to be due to the dry initial state and not due to the radiative transfer calculation. Comparison of the observed and simulated T_{BS} during the passage of the IOP cloud field shows the simulated cloud base to be too warm (low) at first, but within 10 K of the observations at later hours. Errors of 20 K occasionally occur between 2000 and 2300 UTC due to the absence of intermittent stratus in the simulation.

Comparison is also made with theoretical heating rates calculated using the rawinsonde data and measured ice water size distributions near COF. The largest differences between the observed and simulated profiles of solar and infrared heating rates are due primarily to the location and amount of cirrus, and less to the optical properties assigned to the bulk ice water content. The difference between the simulated effective particle radius and that inferred from aircraft data is offset by the high simulated IWC so that the magnitude of the extinction, and thus the heating rates, closely match the theoretical calculations.

Based on this case study, it is concluded that use of the mesoscale case study approach for improving physical parameterizations has difficulties due to the initialization problem. Case studies that utilize increased model resolution are even more difficult to initialize and verify against observations without an accompanying increase in the quality of moisture observations and initial conditions. Studies of cirrus clouds in the mid-latitude winter, such as the Winter Icing and Storms Project (WISP), the International Cirrus Experiment (ICE), the European Cloud and Radiation Experiment (EUCREX), and FIRE are at a particular disadvantage because of the long-range transport by high wind speeds and the poor humidity measurements

and retrievals at cold temperatures. Nevertheless, the model does reproduce many of the dynamical, microphysical, and radiative aspects of the IOP cloud field, both qualitatively and quantitatively. Under these conditions, studies of the sensitivity of cirrus clouds to cloud and radiation parameterizations are a reasonable application of these models. Such sensitivity studies are invaluable for improvement of cloud and radiation parameterizations for numerical weather prediction and for climate modeling.

Acknowledgments. We thank all who made observations or analyzed data for the NASA FIRE-II field program including R. Bergstrom, R. Ferrare, B. Rilling, and S. Sorlie. We also thank W. McKie for programming support. This work is supported by NASA's FIRE-II program and DOE's ARM program, Grant DE-AI05-90ER61074. Computations were carried out at NASA's NAS facility and DOE's NERSC facility.

REFERENCES

Anthes, R. A., E.-Y. Hsie, and Y.-H. Kuo, 1987: Description of the Penn State/NCAR Mesoscale Model Version 4 (MM4). NCAR Tech. Note, NCAR/TN-282, 66 pp. [Available from National Technical Information Service, 5285 Port Royal Rd., Springfield, VA 22161.]

Benjamin, S. G., K. A. Brewster, R. Brummer, B. F. Jewett, T. W. Schlatter, T. L. Smith, and P. A. Stamus, 1991: An isentropic three-hourly data assimilation system using ACARS aircraft observations. *Mon. Wea. Rev.*, **119,** 888–906.

——, T. L. Smith, P. A. Miller, D. Kim, T. W. Schlatter, D. Devenyi, J.-M. Carriere, and R. Bleck, 1993: Recent developments in the MAPS isentropic-sigma data assimilation system. *Idojaras,* **97,** 1–19.

——, and Coauthors, 1994: The Rapid Update Cycle at NMC. Preprints, *10th Conf. on Numerical Weather Prediction,* Portland, OR, Amer. Meteor. Soc., 566–568.

——, G. A. Grell, K. J. Brundage, T. L. Smith, J. M. Brown, T. G. Smirnova, and Z. Yang, 1995: The next version of the Rapid Update Cycle—RUC II. Preprints, *Sixth Conf. on Aviation Weather Systems,* Dallas, TX, Amer. Meteor. Soc., 57–61.

Cairns, M. M., and Coauthors, 1993: A preliminary evaluation of aviation-impact variables derived from numerical models. NOAA Tech. Memo. ERL FSL-5, 165 pp. [Available from NTIS, 5285 Port Royal Road, Springfield, VA 22061.]

Downing, H. D., and D. Williams, 1975: Optical constants of water in the infrared. *J. Geophys. Res.,* **80,** 1656–1661.

Ebert, E. E., and J. A. Curry, 1992: A parameterization of ice cloud optical properties for climate models. *J. Geophys. Res.,* **97,** 3831–3836.

Ferrare, R. A., S. H. Melfi, D. N. Whiteman, and K. D. Evans, 1992: Raman lidar measurements of Pinatubo aerosols over southeastern Kansas during November–December 1991. *Geophys. Res. Lett.,* **19,** 1599–1602.

Fowler, L. D., and D. A. Randall, 1994: Impact of cloud microphysics on cloud-radiation interactions in the CSU GCM. Preprints, *Sixth Conf. on Climate,* Nashville, TN, Amer. Meteor. Soc., 313–317.

Heckman, S. F., and W. R. Cotton, 1993: Mesoscale numerical simulation of cirrus clouds—FIRE case study and sensitivity analysis. *Mon. Wea. Rev.,* **121,** 2264–2284.

Heymsfield, A. J., 1975: Cirrus uncinus generating cells and the evolution of cirroform clouds. *J. Atmos. Sci.,* **32,** 799–805.

——, and L. M. Miloshevich, 1995: Relative humidity and temperature influences on cirrus formation and evolution: Observation from wave clouds and FIRE II. *J. Atmos. Sci.,* **52,** 4302–4326.

——, K. M. Miller, and J. D. Spinhirne, 1990: The 27–28 October 1986 FIRE IFO cirrus case study: Cloud microstructure. *Mon. Wea. Rev.,* **118,** 2313–2328.

Iacobellis, S. F., and R. C. J. Somerville, 1991: Diagnostic modeling of the Indian monsoon onset. Part I: Model description and validation. *J. Atmos. Sci.,* **48,** 1948–1959.

Jensen, E. J., O. B. Toon, D. L. Westphal, S. Kinne, and A. J. Heymsfield, 1994a: Microphysical modeling of cirrus 1: Comparison with 1986 FIRE IFO measurements. *J. Geophys. Res.,* **99,** 10 421–10 442.

——, ——, ——, ——, and ——, 1994b: Microphysical modeling of cirrus 2: Sensitivity studies. *J. Geophys. Res.,* **99,** 10 443–10 454.

Kinne, S., T. P. Ackerman, A. J. Heymsfield, F. P. J. Valero, K. Sassen, and J. D. Spinhirne, 1992: Cirrus microphysics and radiative transfer: Cloud field study on 28 October 1986. *Mon. Wea. Rev.,* **120,** 661–684.

——, ——, M. Shiobara, A. J. Heymsfield, L. Miloshevich, J. Wendell, and R. W. Bergstrom, 1996: Cirrus cloud radiative and microphysical properties from ground observations and in-situ measurements during the FIRE'91 and their application to exhibit problems in cirrus solar radiative transfer modeling. *J. Atmos. Sci.*

Levkov, L., B. Rockel, K. Kapitza, and E. Raschke, 1992: 3D mesoscale numerical studies of cirrus and stratus clouds by their time and space evolution. *Beitr. Phys. Atmos.,* **65,** 35–58.

Mace, G. G., D. O'C. Starr, T. P. Ackerman, and P. Minnis, 1995: Examination of coupling between an upper-tropospheric cloud system and synoptic-scale dynamics diagnosed from wind profiler and radiosonde data. *J. Atmos. Sci.,* **52,** 4094–4127.

Matrosov, S. Y., A. J. Heymsfield, J. M. Intrieri, B. W. Orr, and J. B. Snider, 1995: Ground-based remote sensing of cloud particle sizes during the 26 November 1991 FIRE II cirrus case: Comparisons with in situ data. *J. Atmos. Sci.,* **52,** 4128–4142.

McNally, A. P., and M. Vesperini, 1995: Variational analysis of humidity information from TOVS radiances. EUMETSAT/ECMWF Fellowship Report No. 1, 29 pp. [Available from ECMWF, Shinfield Park, Reading RG2 9AX, United Kingdom.]

Minnis, P., W. L. Smith, Jr., D. F. Young, and P. W. Heck, 1993: Cloud fields derived from satellite and surface data during FIRE Cirrus Phase II. NASA CP 3238, *Proc. FIRE Cirrus Science Conf.,* Breckenridge, CO, NASA, 36–39.

Nieman, S., P. Menzel, C. M. Hayden, S. Wanzong, and C. S. Velden, 1996: Upgrades to the NOAA/NESDIS automated cloud-motion vector system. Preprints, *Eighth Conf. on Satellite Meteorology and Oceanography,* Atlanta, GA, Amer. Meteor. Soc., 1–4.

Painter, L. R., R. D. Birkhoff, and E. T. Arakawa, 1969: Optical measurements of liquid water in the vacuum ultraviolet. *J. Chem. Phys.,* **51,** 243–251.

Palmer, K. F., and D. Williams, 1974: Optical properties of water in the near infrared. *J. Opt. Soc. Amer.,* **64,** 1107–1110.

Pilewskie, P., and F. P. J. Valero, 1993: Ground-based passive remote sensing during FIRE IFO II. NASA CP 3238. *Proc. FIRE Cirrus Science Conf.,* Breckenridge, CO, NASA, 105–106.

Randall, D. A., L.-M. Xu, R. J. C. Somerville, and S. Iacobellis, 1996: Single-column models and cloud ensemble models as links between observations and climate models. *J. Climate,* **9,** 1683–1697.

Roberts, R. E., J. E. A. Selby, and L. M. Biberman, 1976: Infrared continuum absorption by atmospheric water vapor in the 8–12-μm window. *Appl. Opt.,* **15,** 2085–2090.

Rockel, B., E. Raschke, and B. Weyres, 1991: A parameterization of broad band radiative transfer properties of water, ice, and mixed clouds. *Beitr. Phys. Atmos.,* **64,** 1–12.

Rothman, L. S., 1983: AFGL atmospheric line parameters compilation: 1982 edition. *Appl. Opt.,* **22,** 2247–2256.

Sagan, C., and J. Pollack, 1967: Anisotropic nonconservative scattering and the clouds of Venus. *J. Geophys. Res.,* **72,** 469–477.

Shaw, J. A., J. B. Snider, J. H. Churnside, and M. D. Jacobson, 1995: Comparison of infrared atmospheric brightness temperatures measured by a fourier transform spectrometer and a filter radiometer. *J. Atmos. Oceanic. Technol.,* **12,** 1124–1128.

Shiobara, M., J. D. Spinhirne, A. Uchiyama, and S. Asano, 1996: Optical depth measurements of aerosol, cloud, and water vapor using sun photometers during FIRE Cirrus IFO II. *J. Appl. Meteor.,* **35,** 36–46.

Slingo, A., R. C. Wilderspin, and R. N. B. Smith, 1989: Effect of improved physical parameterizations on simulations of cloudiness and the earth's radiation budget. *J. Geophys. Res.,* **94,** 2281–2301.

Soden, B. J., and F. P. Bretherton, 1993: Upper tropospheric relative humidity from GOES 6.7 μm channel method and climatology for July 1987. *J. Geophys. Res.,* **98,** 16 669–16 688.

——, S. A. Ackerman, D. O'C. Starr, S. H. Melfi, and R. A. Ferrare, 1994: Comparison of upper tropospheric water vapor from GOES, Raman lidar, and Cross-Chain Loran Atmospheric Sounding System measurements. *J. Geophys. Res.,* **99,** 21 005–21 106.

Stackhouse, P. W., Jr., and G. L. Stephens, 1991: A theoretical and observational study of the radiative properties of cirrus: Results from FIRE 1986. *J. Atmos. Sci.,* **48,** 2044–2059.

Starr, D. O'C., and D. P. Wylie, 1990: The 27–28 October 1986 FIRE cirrus case study: Meteorology and clouds. *Mon. Wea. Rev.,* **118,** 2259–2287.

Stokes, G. M., and S. T. Schwartz, 1994: The atmospheric radiation measurement (ARM) Program: Programmatic background and design of the cloud and radiation test bed. *Bull. Amer. Meteor. Soc.,* **75,** 1201–1220.

Sun, Z., and K. P. Shine, 1994: Studies of the radiative properties of ice and mixed-phase clouds. *Quart. J. Roy. Meteor. Soc.,* **120,** 111–137.

Takano, Y., and K.-N. Liou, 1989: Solar radiative transfer in cirrus clouds. Part I: Single-scattering and optical properties of hexagonal ice crystals. *J. Atmos. Sci.,* **46,** 488–492.

Toon, O. B., C. P. McKay, T. P. Ackerman, and K. Santhanam, 1989: Rapid calculation of radiative heating rates and photodissociation rates in inhomogeneous multiple scattering atmospheres. *J. Geophys. Res.,* **94,** 16 287–16 301.

Uttal, T., E. E. Clothiaux, T. P. Ackerman, J. M. Intrieri, and W. L. Eberhard, 1995: Cloud boundary statistics during FIRE II. *J. Atmos. Sci.,* **52,** 4264–4275.

Wade, C. G., 1991: Improved low humidity measurements using the radiosonde hygristor. Preprints, *Seventh Symp. on Meteorological Observations and Instrumentation,* New Orleans, LA, Amer. Meteor. Soc., 295–290.

Warren, S. G., 1984: Optical constants of ice from the ultraviolet to the microwave. *Appl. Opt.,* **23,** 1206–1226.

Westphal, D. L., 1996: Uncertainties in converting NWS radiosonde hygristor resistance to relative humidity: Illustration using the FIRE-II dataset. *J. Atmos. Oceanic Technol.*

Zhang, D.-L., 1989: The effect of parameterized ice microphysics on the simulation of vortex circulation with a mesoscale hydrostatic model. *Tellus,* **41A,** 132–147.